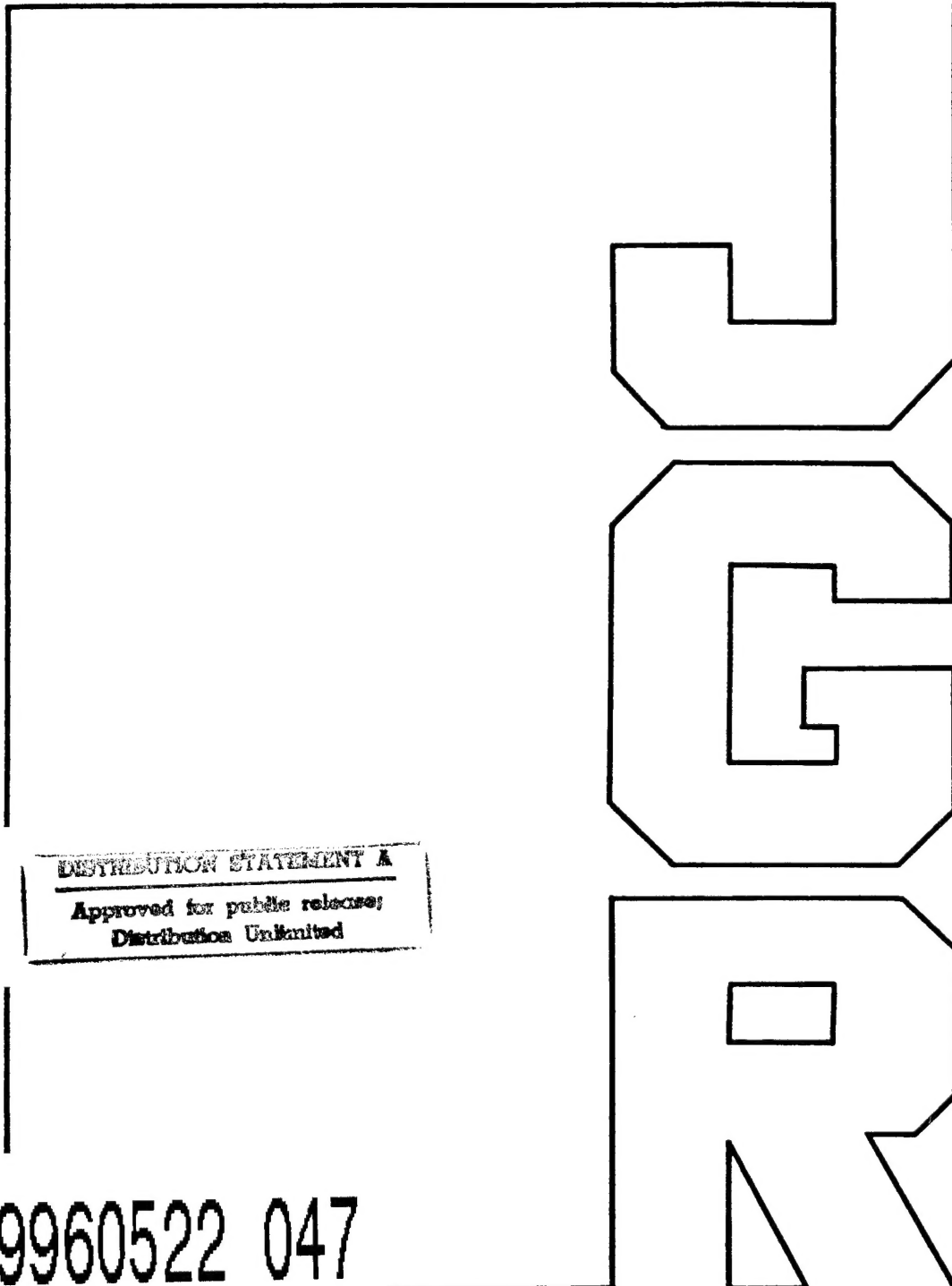


An examination of the North Pacific Ocean in the  
spectral domain using Geosat altimeter data and a  
numerical ocean model

G. A. Jacobs, W. J. Teague, J. L. Mitchell , and H. E. Hurlburt

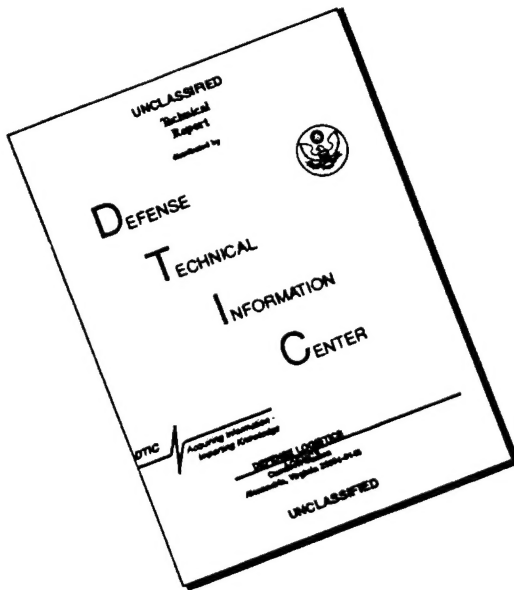


19960522 047

JOURNAL OF GEOPHYSICAL RESEARCH, VOL. 101, NO. C1, PAGES 1025-1044, JANUARY 15, 1996

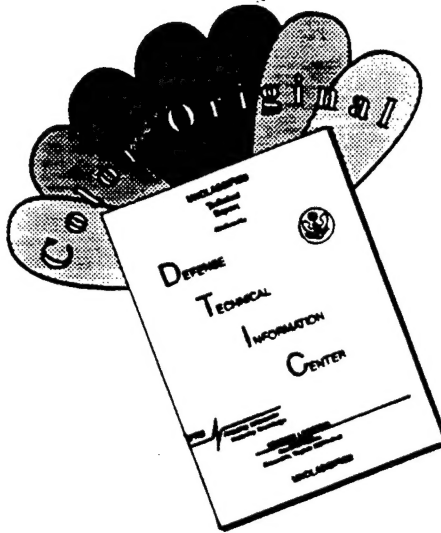
DTIC QUALITY INSPECTED 1

# DISCLAIMER NOTICE



THIS DOCUMENT IS BEST  
QUALITY AVAILABLE. THE COPY  
FURNISHED TO DTIC CONTAINED  
A SIGNIFICANT NUMBER OF  
PAGES WHICH DO NOT  
REPRODUCE LEGIBLY.

# DISCLAIMER NOTICE



THIS DOCUMENT IS BEST  
QUALITY AVAILABLE. THE COPY  
FURNISHED TO DTIC CONTAINED  
A SIGNIFICANT NUMBER OF  
COLOR PAGES WHICH DO NOT  
REPRODUCE LEGIBLY ON BLACK  
AND WHITE MICROFICHE.

# An examination of the North Pacific Ocean in the spectral domain using Geosat altimeter data and a numerical ocean model

G. A. Jacobs, W. J. Teague, J. L. Mitchell<sup>1</sup>, and H. E. Hurlburt

Naval Research Laboratory, Stennis Space Center, Mississippi

**Abstract.** The sea surface height (SSH) variations of the North Pacific ocean and the Kuroshio Extension region, in particular, are examined by frequency and wavenumber decompositions of a 1/8°, six-layer primitive equation Pacific Ocean model and of the Geosat Exact Repeat Mission (ERM) data. Both data sets exhibit peaks in variability at 1 and 2 cycles per year over much of the Kuroshio Extension region. This study is restricted to these two frequencies. Annual variations of equatorial currents in both data sets are similar in both space and time, with the variations in the South Equatorial Current appearing as annual westward propagations. Annual variations in the strength of the Kuroshio Extension are manifested mainly through changes in the strength of the recirculation gyres on the southern side of the current. Annual transport maxima for the Kuroshio Extension occur around late October for both the model and Geosat. Large-scale variations (length scales greater than 1000 km) of the model and Geosat have comparable amplitudes. The main differences between the model SSH and the Geosat ERM data occur over regions where seasonal steric variations are significant (from 20°N to 30°N). Wavenumber spectra over the Kuroshio Extension region reveal similar dynamics in both data sets. Much of the energy in wavenumber spectra appears as westward propagating SSH anomalies near the theoretical Rossby wave dispersion relations. As the Rossby wave dispersion relation changes with latitude (shifting to shorter wavelengths with higher latitudes), the peaks in the wavenumber decompositions follow. Thus the dynamics are generally consistent with quasi-geostrophic dynamics in both the model and altimeter data. Wavelengths of propagating SSH anomalies which have spectral peaks near the Rossby dispersion curve are longer in the Geosat and model than wavelengths indicated by theory. In the semiannual frequency below 35°N, westward propagation dominates over eastward propagation in both Geosat and the model. Most differences in the dynamics of the model and Geosat occur at shorter length and timescales, with Geosat showing higher amplitudes at the shorter scales than the model.

## 1. Introduction

Recent numerical experiments by *Hurlburt et al.* [this issue] have shown which physical properties of the Pacific Ocean are significant for obtaining a realistic pattern of mean currents over the North Pacific Ocean basin. High horizontal resolution (permitting vigorous eddy activity), multiple layers, realistic bottom topography, and appropriate entrainment/detrainment schemes have all been found necessary to reproduce the

mean Kuroshio Extension and Oyashio current systems in addition to mean equatorial current systems. One purpose of this study is to determine if the physical parameters included in the ocean model are sufficient to also accurately reproduce the temporal variations of the current systems through comparison with Geosat altimetry. In addition, the model provides a source of information to corroborate results inferred from the altimeter data. Thus the model and altimeter data substantiate each other and strengthen conclusions derived from their combination.

To determine the accuracy of the model, Geosat Exact Repeat Mission (Geosat ERM) data are used. Though there are many data sets available for comparison, altimeter data compose the only quantitative data set with sufficiently large and uniform space-time coverage. Currently, other altimeter data sets are available (TOPEX/POSEIDON and ERS 1). We have chosen

<sup>1</sup>Also at Colorado Center for Astrodynamics Research, University of Colorado, Boulder.

This paper is not subject to U.S. copyright. Published in 1996 by the American Geophysical Union.

Paper number 95JC02081.

the Geosat ERM to balance the trade-offs between two quantities: the spatial resolution and the number of repeat passes. The Geosat ERM has approximately twice the spatial resolution of TOPEX/POSEIDON. This permits a larger expanse of wavenumber space to be viewed (up to about 5 cycles/1000 km as opposed to 3 cycles/1000 km for TOPEX/POSEIDON). The number of repeat passes from the Geosat ERM is greater than that of ERS 1. This results in more accurate statistics (mean, annual and semiannual cycle estimates) at each point along the ground track. Obviously, a study of different space and timescales may require a balance provided by one of the other altimeter satellites.

As sea surface height (SSH) variations are the prime data type available from Geosat, model examination is restricted to SSH. Simulated altimeter data are sampled from the primitive equation North Pacific basin model in the same manner as the Geosat ERM. As discussed in section 2, the model is forced by realistic winds and the altimetric sampling matches the Geosat data in space and time. This allows identical analyses of the two data sets. Comparison of only SSH is not a full validation of the model. There is much subsurface information (such as the equatorial undercurrent) which cannot be observed from the SSH alone. However, many studies have been made which relate SSH to subsurface information. These studies have been made from both observational data [Carnes and Mitchell, 1990; Carnes et al., 1994] and from numerical model experiments [Hurlburt, 1986; Hurlburt et al., 1990]. In general, midlatitudes indicate good correlation between the surface and subsurface information, while equatorial regions indicate less correlation.

There are several approaches available for comparing temporal variability. One method compares statistics of the two data sets in time and space. This approach is taken by Mitchell et al. [this issue]. In this study, SSH variability is analyzed through frequency-wavenumber decomposition. This simplifies the comparison of the dynamics contained in each data set with idealized theory. For example, dispersion relations from simplified dynamics are easily displayed and understood in frequency-wavenumber space. Identification of different dynamical regimes caused by bathymetry such as the Shatsky Rise [Mizuno and White, 1983] can also be simplified by this method. All of the information contained in the original data is preserved in the frequency-wavenumber transform if a proper discretization and a sufficiently large expanse of frequency-wavenumber space is used.

A frequency analysis is made first with results showing peak variability at 1 and 2 cycles per year (cpy) in both the Geosat and model data, in agreement with previous studies [Zlotnicki, 1991; Chelton et al., 1990; Zlotnicki et al., 1989]. This study is an attempt to understand the variability at only these two frequencies. Maps of amplitude and phase of the spatial variability at these frequencies are constructed to show seasonal fluctuations of SSH due to equatorial currents and variations in the strength of the Kuroshio Extension.

To compare propagation characteristics, wavenumber

decomposition of the amplitude and phase of the two frequencies is performed over the Kuroshio Extension region which is rich in eddy and current meandering activity. Care is required in decomposing over this sub-region because of the sharp spatial changes in dynamical structure [Hall, 1991; Qiu et al., 1991]. The immediate region of the Kuroshio Extension is dominated by meandering currents and eddy-shedding events, while a few hundred kilometers from the stream, the dynamics are quite different. Thus considerably different dynamical spectra could exist at each point in space. The choice of the region size for the wavenumber decomposition is a compromise between two effects. If a wavenumber-frequency spectra of the entire region is constructed, it would contain the same information contained in the many spectra produced over small regions, but the individual spectral characteristics would be averaged together and the ability to distinguish various dynamical regions would be lost. Owing to discretized sampling, the smaller the region over which a wavenumber decomposition is made, the cruder the resolution obtained in the spectra. We have tried to balance these two effects by computing spectra over  $10^6$  square regions. Resulting wavenumber spectra are compared to the linear Rossby wave dispersion relation (which varies from one point in space to another) at each frequency. Energy in the wavenumber spectra appears mostly as westward propagating SSH anomalies, with wavelengths decreasing with increasing latitude in both the model and the Geosat data.

Realistically, we cannot expect spectra of the numerical simulations and Geosat data to match exactly. The model cannot reproduce all scales of ocean variability. Simplifications in the model's dynamics are necessary to allow solution of model equations on present computers and to exclude dynamics which are not of direct interest. Altimeter data contain measurement errors such as those due to poorly estimated atmospheric effects [Emery et al., 1990], orbit errors [Tai, 1989], aliasing problems due to time-space sampling [Jacobs et al., 1992], and tide model errors [Cartwright and Ray, 1990]. A test of the wavenumber spectra is made to show where the dynamics of the model and Geosat data differ significantly. The dynamics of the two data sets agree well on large scales (greater than 1000 km), with increasing dissimilarities at shorter length scales. The differences are partly due to flow instabilities which are not deterministic based on wind forcings.

An overview of the model and the Geosat data processing is given in section 2. An initial comparison of frequency spectra showing the dominance of the annual and semiannual frequencies is discussed in section 3. The results of the spatial amplitude and phase of the annual and semiannual frequencies are discussed in section 4. A discussion of the wavenumber decomposition is contained in section 5.

## 2. The Model and the Geosat Data

The simulated SSH variability used in this study is derived from the North Pacific (NPAC) six-layer prim-

itive equation model [Hurlburt *et al.*, this issue]. This model is an evolution from that of Hurlburt and Thompson [1980] as expanded by Wallcraft [1991].

The model is an isopycnal model, providing a vertical discretization through a layered formulation in which variables represent a vertical average over each layer. The pressure anomaly of each layer gives a direct calculation of layer thickness, and the layer thicknesses are summed over all six layers to produce a sea surface height. Space-time mean layer interface depths are chosen at 135, 320, 550, 800, and 1050 m, but large deviations from these depths occur in the temporal variability and spatially in the temporal mean. Densities are held constant within each layer in both space and time. An eddy viscosity of  $100 \text{ m}^2 \text{s}^{-1}$  is employed (i.e., low enough to permit vigorous flow instabilities and numerous eddies).

The NPAC model domain covers the North Pacific basin north of  $20^\circ\text{S}$  at a horizontal resolution of  $0.125^\circ \times 0.176^\circ$  (latitude, longitude). The 200-m isobath is selected to define the lateral boundaries of the model except at a few particular points such as the Tsushima and Tsugaru Straits which are open to allow flow through the Sea of Japan. A closed boundary is imposed at  $20^\circ\text{S}$ . Digitized realistic bottom topography based on the  $1/12^\circ$  ETOP 05 bathymetry [National Oceanic and Atmospheric Administration (NOAA), 1986] is embedded in the lowest layer at the model resolution.

To spin up, the model is run at  $1/4^\circ$  horizontal resolution for 40 model years. The model resolution is then changed to  $1/8^\circ$  horizontal resolution, and the model run is continued for 11 model years. During this spin-up, the model was forced by the Hellerman and Rosenstein [1983] wind stress climatology. After spin-up, the model is driven by surface wind stress from daily averaged European Centre for Medium-Range Weather Forecasts (ECMWF) 1000-mbar winds during the period 1981–1992. The ECMWF annual mean over the 1981–1991 time period is replaced by that from the Hellerman–Rosenstein climatology. The replacement of the ECMWF annual mean with the annual mean of Hellerman–Rosenstein minimizes transient effects which occur when wind forcings are changed from the climatological Hellerman–Rosenstein to the observed ECMWF.

The model time step is 0.4 hours, and while the model is running, model SSH is sampled in space and time in the same manner as the Geosat sampling. This sampling resulted in time series of SSH at points spaced about 7 km along ground tracks.

For additional model–data comparisons and more discussion of this and earlier simulations, see Hurlburt *et al.* [this issue] and Mitchell *et al.* [this issue]. Hurlburt *et al.* show which Pacific Ocean physical and dynamical characteristics are important in producing realistic Kuroshio Extension and Oyashio current systems. Through a series of model experiments, bottom topography, nonlinear dynamics, and high horizontal resolution are found to be essential to the dynamics of the Kuroshio Extension. Mitchell *et al.* find that the SSH variability along the Kuroshio Extension is linked to the mean abyssal currents and bottom topography gradients.

These authors demonstrate that the NPAC model realistically reproduces the major Pacific currents including the equatorial systems, the northern subtropical gyre, the subarctic gyre, and the Kuroshio and Oyashio Currents.

The Geosat data consist of geophysical data records (GDRs) produced by NOAA. The SSH data are corrected for the effects of dry troposphere, wet troposphere, ionosphere, inverse barometer, and electromagnetic bias [Cheney *et al.*, 1987]. Errors in the orbit solutions based on the Goddard Earth Model (GEM-T2) gravity model [Haines *et al.*, 1990] are minimized by removing a once per revolution sinusoid fit to the collinear repeat passes. Tidal contamination is removed using the Schwiderski [1980a,b] tide model. A global algorithm is employed to remove the residual effects of  $M_2$  tidal aliasing (due to errors in the Schwiderski model) which appear at a frequency of 1.15 cpy [Jacobs *et al.*, 1992]. Tide models more accurate than the Schwiderski model are available [Cartwright and Ray, 1990; Egbert *et al.*, 1994]. However, any tide model will contain errors which have a high probability of appearing as baroclinic Rossby waves in Geosat data [Jacobs *et al.*, 1992; Schlax and Chelton, 1994]. The method used to remove tide contamination removes any variability which appears as tide alias. Thus energy appearing as Rossby waves will not be due to tide aliasing. The particular points in wavenumber–frequency space at which the tide aliases occur (and therefore at which true oceanographic variability may be removed) are accurately known. The tide aliases to a wavenumber of about 2 cycles per 1000 km in a direction northwest (perpendicular to descending tracks) and southwest (perpendicular to ascending tracks).

The resulting data set consists of SSH time series every 7 km along the Geosat ground tracks. For further details on the Geosat data processing, see Jacobs *et al.* [1992]. Data from both ascending and descending ground tracks are employed in the analyses (see Figure 1). Outlying data are identified by inspecting the SSH time series at each point along the ground track. If a value of SSH falls more than 4 standard deviations from the mean of the time series in which it is contained, it is removed as an outlier. In general, less than 1% of the altimeter data is removed in this manner. The model data do not have outliers as do the Geosat data.

### 3. Frequency Analysis

Only frequencies at which the relative maximum variability is observed are examined in this study. A complete frequency–wavenumber decomposition of either the Geosat data or the model would be computationally cumbersome, and the results would be difficult to present (even two frequencies are a challenge to present clearly and understandably). To identify dominant timescales in the data sets, a frequency decomposition of the SSH anomalies relative to their 3-year (1987–1989) mean is performed. Normal Fourier decomposition methods cannot be employed due to missing Geosat data. Instead, a least squares approach is taken in

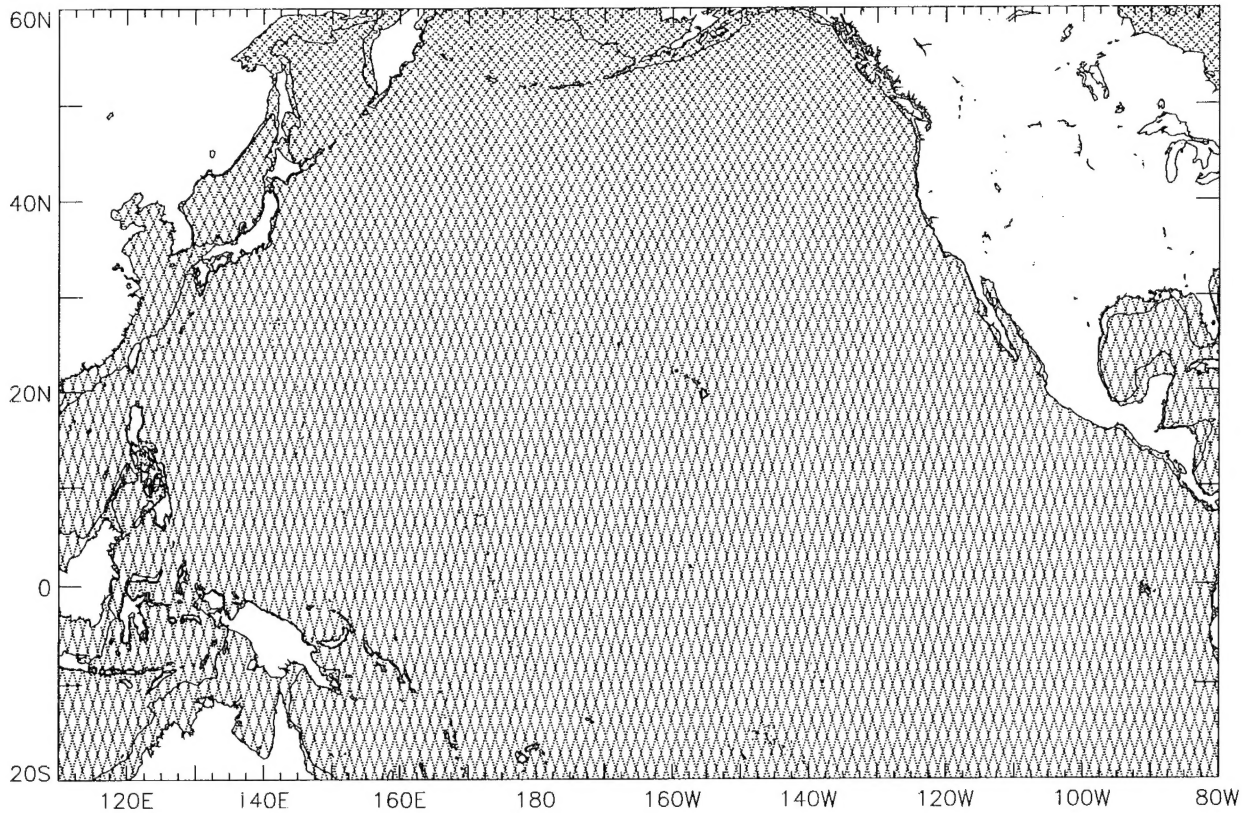


Figure 1. Ground tracks of the Geosat Exact Repeat Mission in the North Pacific Basin. The distance between ground tracks is about 150 km at the equator, and points are sampled every 7 km along the tracks every 17.05 days. The 200-m isobath is the boundary of the numerical model, and the model was sampled on these tracks in a manner identical to the Geosat altimeter's sampling scheme.

which a constant, a linear trend in time, and a sinusoid are fit to the time series of SSH at each point along the ground tracks to determine the amplitude and phase at frequencies extending from 0.5 to 6 cpy at increments of 0.1 cpy. Note that leakage of peaks occurs at about 1/3 cpy (since the time series is approximately 3 years long), so peaks separated by more than this amount are not due to leakage of energy. The linear trend is included to prevent energy from long time periods (longer than the 3 year data set) leaking to other frequencies. A similar analysis is performed for the model SSH anomalies.

The least squares harmonic fit produces results equivalent to discrete Fourier transforms if no data are missing. Gaps in the Geosat data may cause some frequency aliasing. However, care is taken to insure a minimum number of measurements exist at each ground track point before making estimates of the spectra by examining the expected errors of the least squares fit. Once the amplitude spectra are determined at each ground track point, the spectra are averaged over  $10^\circ$  squares and the amplitudes plotted as a function of frequency for each square. This process averages about 2000 spectra from 14 separate ground tracks over each  $10^\circ$  square. The results are presented in Figures 2a and 2b for Geosat and the model, respectively.

Geosat and model spectra are both red (i.e., energy is concentrated at lower frequencies), with the model spectra redder than the Geosat spectra. This is prob-

ably due to noise of the order of 2 to 4 cm amplitude at each frequency in the Geosat data. Both data sets show relatively large peaks at 1 and 2 cpy in most of the  $10^\circ$  squares. These peaks are separated by more than the leakage length scale (1/3 cpy) so are not caused by leakage between them or by leakage from lower frequencies. Geosat data also show peaks at 3 and 4 cpy but not as large as the 1 and 2 cpy peaks. Some decrease in energy past 4 cpy exists in the Geosat spectra, while the model shows a fairly flat low-energy spectrum at frequencies higher than 4 cpy. The Nyquist frequency for the Geosat sampling is about 10 cpy. On the basis on the roll-off rates at frequencies greater than 4 cpy, only a small fraction of the model energy is aliased from frequencies higher than 10 cpy. The Geosat data imply more energy at the higher frequencies and thus a larger amount of aliasing.

Annual peaks are largest in the Kuroshio Extension (from  $30^\circ$ N to  $40^\circ$ N) in both data sets. The spectra show the most rapid low-frequency roll-off (decrease in amplitude with respect to frequency) in this region. Amplitudes decrease toward the east (away from the separation point of the Kuroshio Current) at all latitudes but most significantly over the Kuroshio Extension. As the 1 and 2 cpy frequencies contain the most consistent local maxima over the region, the remainder of the analysis is confined to these two frequencies.

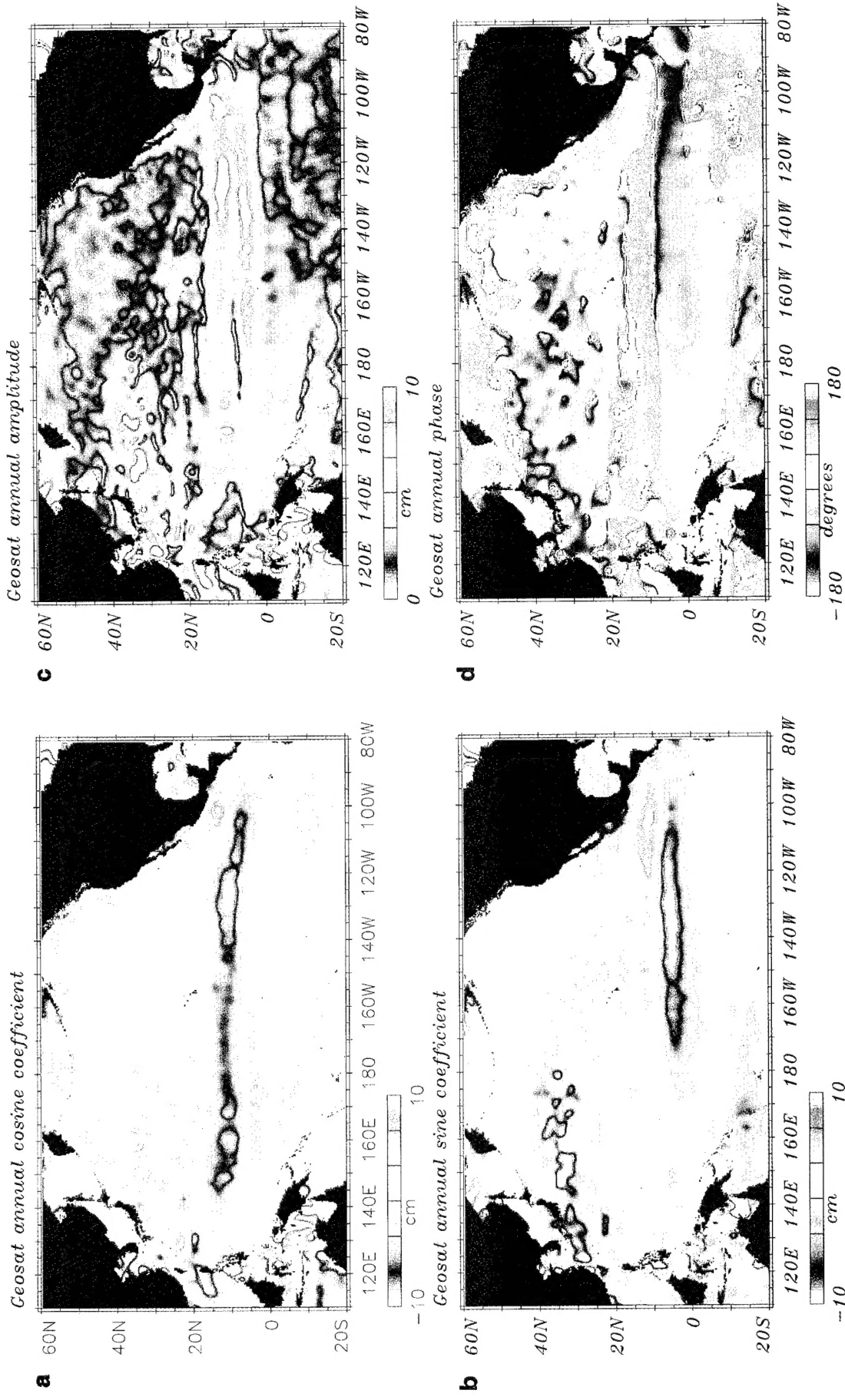


Plate 1a. Cosine coefficient of the annual signal of the Geosat data. The low at  $12^{\circ}$  N and high at  $20^{\circ}$  N indicate a maximum intensity in the North Equatorial Current (NEC) at  $15^{\circ}$  N during January.

Plate 1b. Sine coefficient of the annual signal of the Geosat data. The negative region between  $30^{\circ}$  N to  $35^{\circ}$  N and  $140^{\circ}$  E to  $160^{\circ}$  E is the area of the Kuroshio Extension recirculation gyres. These gyres are mainly wind forced and cause a maximum transport in the Kuroshio Extension during the fall.

Plate 1c. Amplitude of the annual signal of the Geosat data. Amplitude peaks occur over the equatorial currents and over the Kuroshio Extension.

Plate 1d. Phase of the annual signal of the Geosat data. The  $180^{\circ}$  phase at  $12^{\circ}$  N indicates a maximum in the NEC intensity during January. The westward increasing phase along the equator implies that the SEC does not intensify as a whole but has a propagating characteristic.

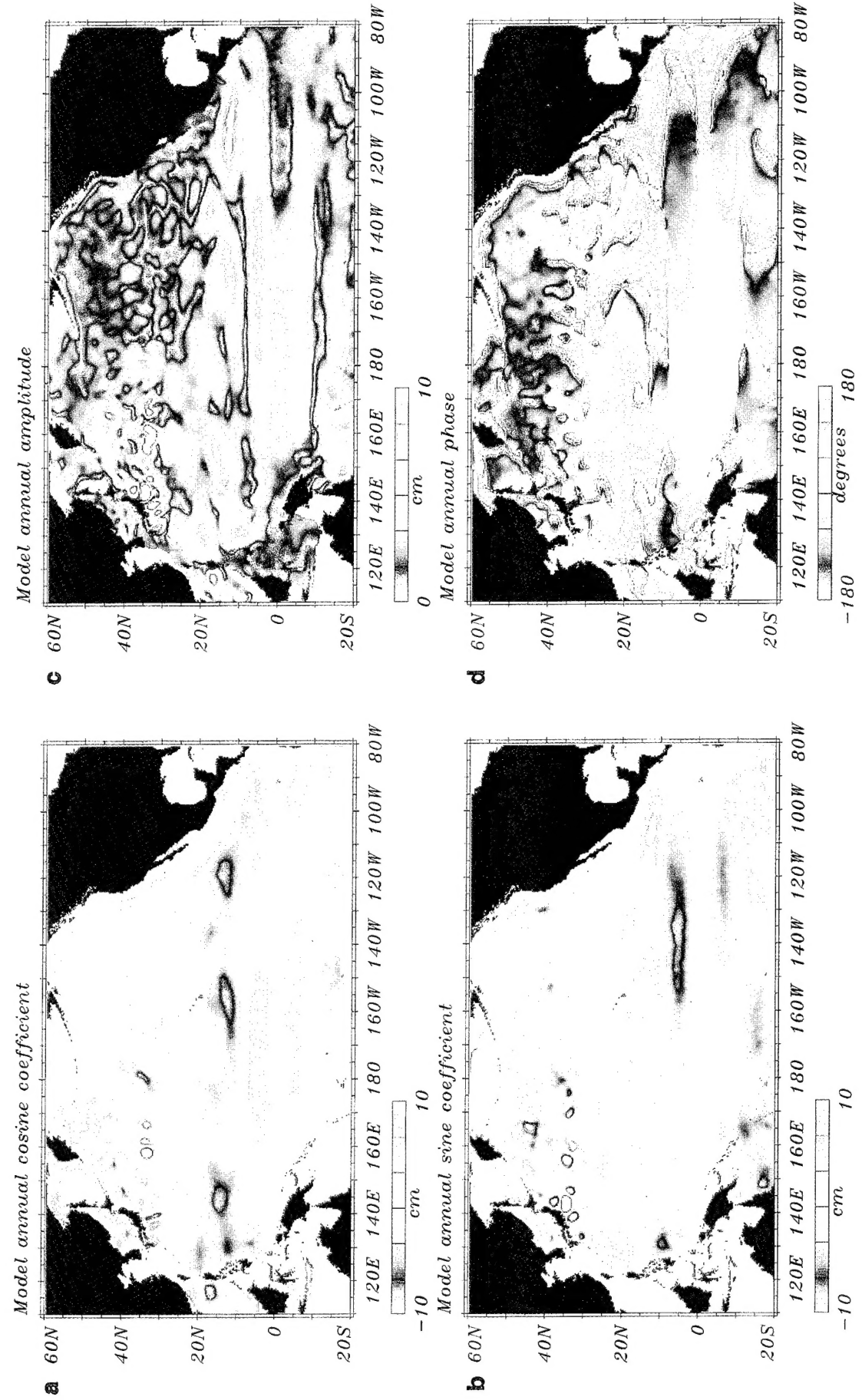


Plate 2a. Cosine coefficient of the annual signal of the six-layer model.

Plate 2b. Sine coefficient of the annual signal of the six-layer model.

Plate 2c. Amplitude of the annual signal of the six-layer model.

Plate 2d. Phase of the annual signal of the six-layer model.

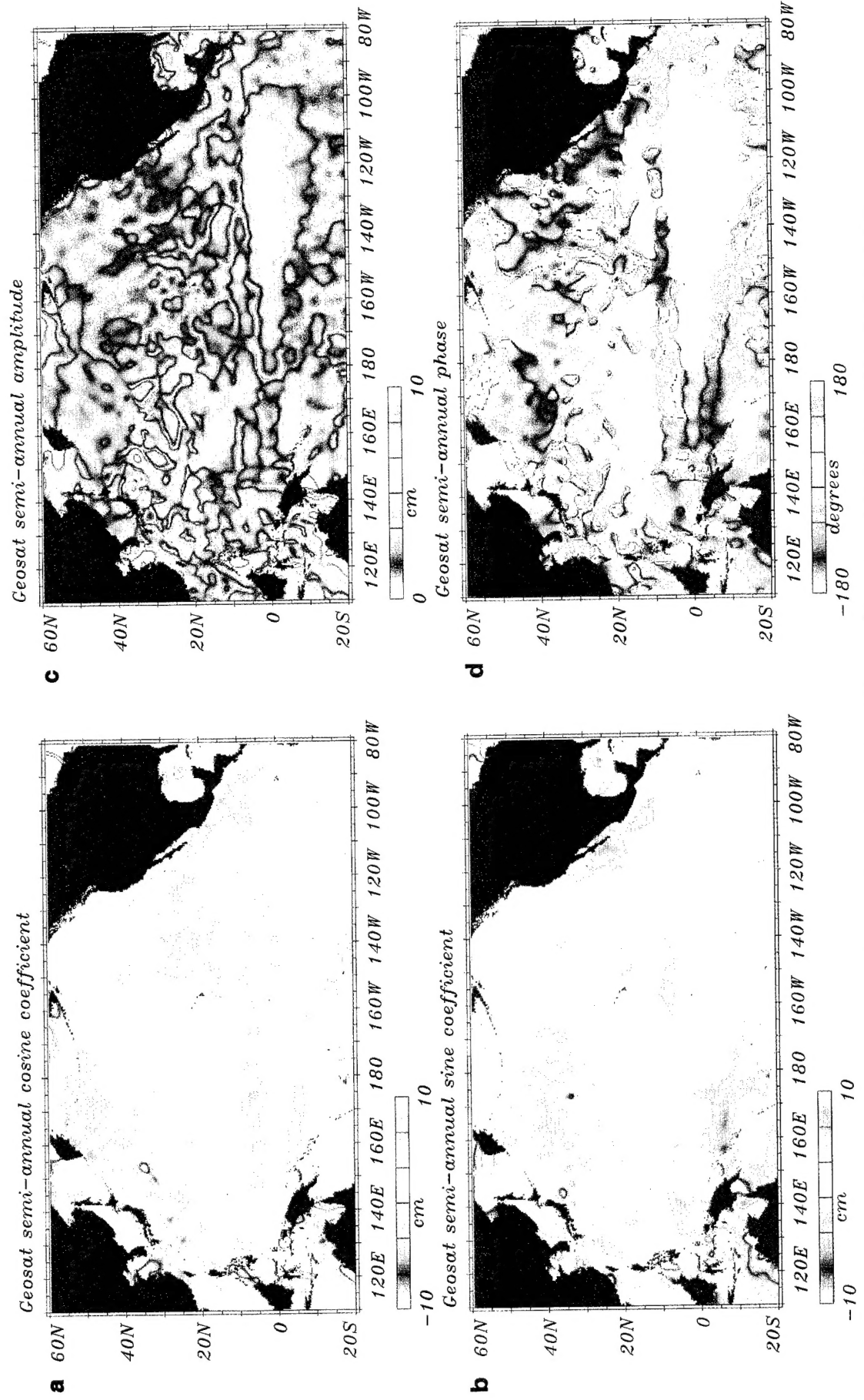


Plate 3. (a) Cosine coefficient, (b) sine coefficient, (c) amplitude, and (d) phase of the semiannual signal of the Geosat data. Amplitudes in both the Geosat and model semiannual signals (Plates 3c and 4c) are very low, and much of the phase (Plates 3d and 4d) at first appears to be noise. However, the spatial scales in the cosine and sine coefficients (Plates 3a, 3b, 4a, and 4b) are larger than the interpolation length used (100 km), and the semiannual phase of the two data sets (Plates 3d and 4d) share westward propagating characteristics which vary in latitude as expected by Rossby waves (Figure 4). The westward propagating character exists mainly above 10° and below 35°. The westward increasing phase ends at 35° N (the theoretical limit for semiannual Rossby waves), and the spatial characteristics of the phase change to much larger scale above this critical latitude.

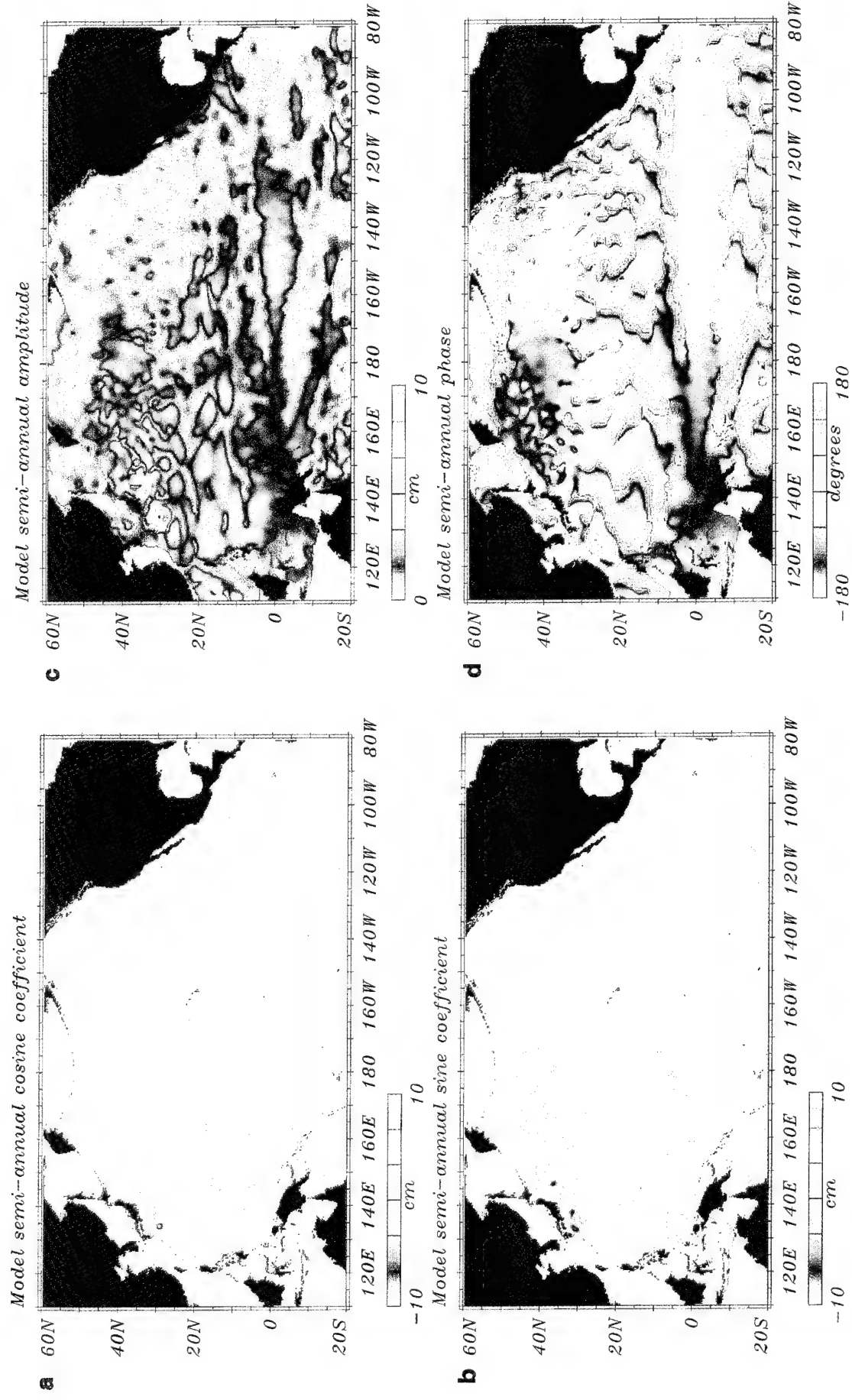
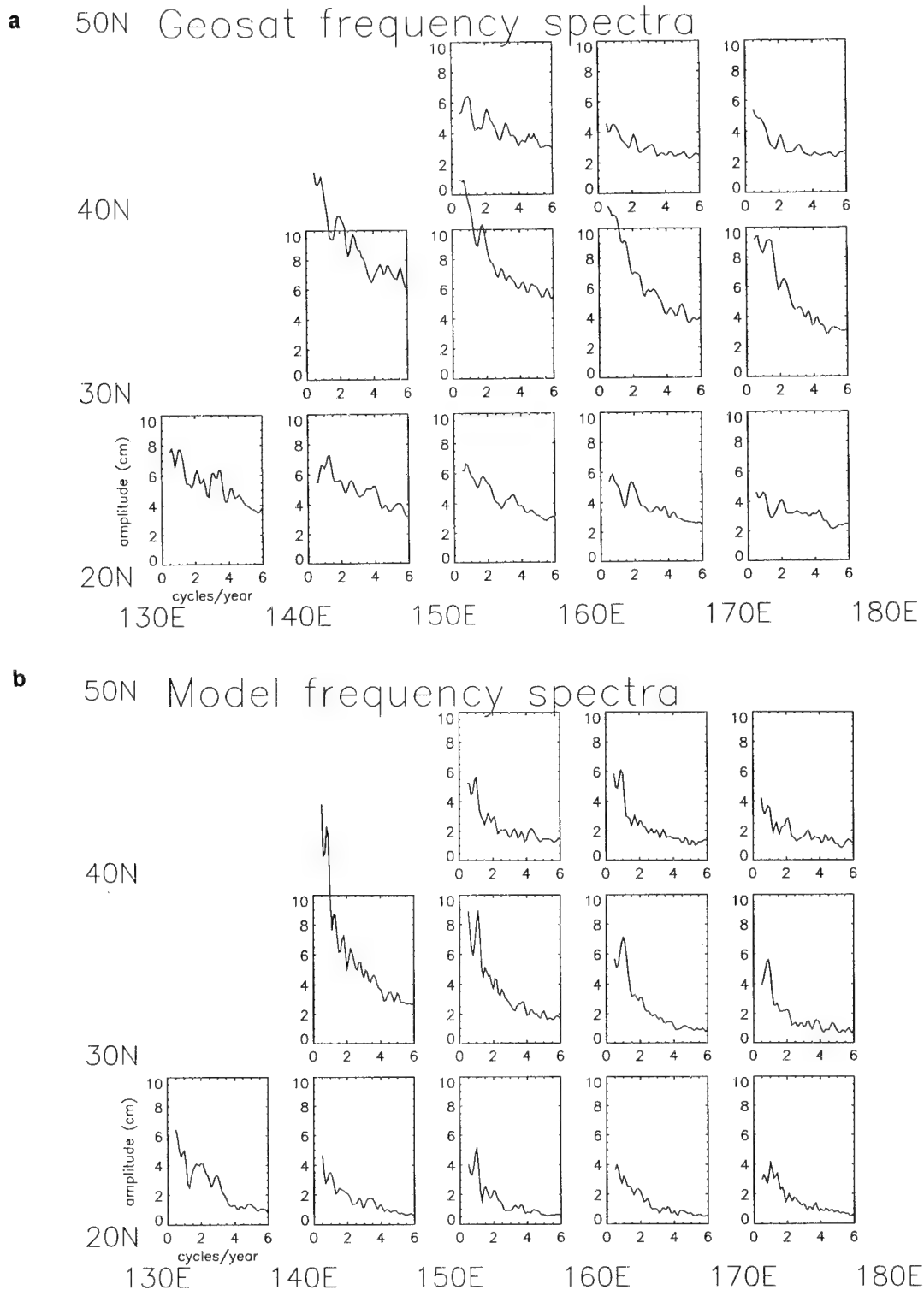


Plate 4a. Cosine coefficient of the semiannual signal of the six-layer model. See discussion of Plate 3a.

Plate 4b. Sine coefficient of the semiannual signal of the six-layer model. See discussion of Plate 3a.

Plate 4c. Amplitude of the semiannual signal of the six-layer model. See discussion of Plate 3a.

Plate 4d. Phase of the semiannual signal of the six-layer model. See discussion of Plate 3a.



**Figure 2.** Amplitude spectra in frequency space of (a) Geosat data and (b) the six-layer model. Spectra are computed from the time series at each point along the sampling ground tracks of Geosat by least squares fitting and then averaged over  $10^\circ$  square regions. The Geosat data show a noise floor of about 2 to 4 cm amplitude. Most spectra of both data sets indicate relative peaks at the annual and semiannual (1 and 2 cycles per year) frequencies. Thus we closely examine only these two frequencies in the remainder of the study.

#### 4. Amplitude and Phase Maps

The results of section 3 indicate relative peaks in both model and Geosat SSH anomaly spectra at the annual and semiannual frequencies. In this section the model

and the Geosat data are compared at these specific frequencies.

The spatial structures of the annual and semiannual frequencies are constructed from annual and semiannual sinusoid fits to the SSH time series at each point

along the ground tracks. At each ground track point a constant, linear trend in time and cosine and sine coefficients for 1 and 2 cpy are least squares fit to the time series of SSH. The linear trend is included to prevent variations at time periods longer than the 3 years of data leaking to the annual and semiannual frequencies. The resulting sine and cosine coefficients are interpolated using a Gaussian-weighted averaging technique [Vazquez *et al.*, 1990] with a length scale of 100 km. For interpolation to a regular  $1/8^\circ$  grid all data within 300 km of a grid element are used in the averaging. From the interpolated sines and cosines, maps of amplitude and phase are constructed. More details on this process are given by Jacobs *et al.* [1992]. The structure of the annual frequency is presented in Plates 1a-1d for Geosat and Plates 2a-2d for the model, and the semianual is presented in Plates 3a-3d for Geosat and Plates 4a-4d for the model.

The time variations of each frequency may be observed from the cosine and sine coefficients. At time 0 (January 1) the SSH amplitude for a particular frequency is given by the cosine coefficient, one quarter cycle later by the sine coefficient, halfway through the cycle by the negative of the cosine, and at three quarters of a cycle by the negative of the sine. Alternatively, variations may be observed from the amplitude and phase maps. Amplitude peaks in Plates 1c, 2c, 3c, and 4c indicate where the majority of the variability occurs. The RMS variability of each frequency is the amplitude divided by  $\sqrt{2}$ . The timing of the highs and lows in SSH anomaly at a given point is indicated by the phase (Plates 1d, 2d, 3d, and 4d). At time 0, points with a phase of 0 have a positive SSH anomaly with an amplitude given by the amplitude plot. Points with a phase of 180 or -180 have a negative SSH with an amplitude given by the amplitude plot. As time increases, the phase at which the SSH reaches its maximum increases. This implies that wave crests propagate toward increasing phase.

The best agreement between the model and Geosat variations occurs in the equatorial regions. Variations in the area from  $15^\circ\text{S}$  to  $15^\circ\text{N}$  are strongly related to large-scale wind forcing. Thus annual variations in wind forcing should produce similar results in the data sets, provided wind forcing, the model response, and the altimeter data are of sufficient accuracy. The cosine and sine coefficients of the annual frequencies for both data sets are similar. Both annual cosine coefficients (Plates 1a and 2a) show two high SSH bands (one at  $5^\circ\text{N}$  and the other at  $5^\circ\text{S}$ ) stretching from  $150^\circ\text{E}$  to  $120^\circ\text{W}$ . The two high bands are separated by a depression along the equator. The annual sine coefficients (Plates 1b and 2b) show two high bands, one stretching from the Gulf of Tehuantepec off the coast of Mexico at  $15^\circ\text{N}$  to just north of New Guinea at  $5^\circ\text{N}$  and another band stretching from the east coast of New Guinea at  $5^\circ\text{S}$  to  $10^\circ\text{S}$  at  $160^\circ\text{W}$ . A low band is sandwiched between the two highs in the sine coefficients.

These equatorial bands are the surface signatures of the annual variations of the equatorial currents. In the annual amplitude plots (Plates 1c and 2c), two high-

amplitude bands stretch across the Pacific at  $5^\circ\text{N}$  and  $12^\circ\text{N}$  in the Geosat and model annual signals. These two bands are the annual strengthening and weakening of the North Equatorial Current (NEC) and the North Equatorial Countercurrent (NECC). The NEC at  $15^\circ\text{N}$  is observed to have a maximum intensity in the winter (around January) evidenced by the low at  $12^\circ\text{N}$  and high at  $20^\circ\text{N}$  in the cosine coefficients (Plates 1a and 2a) and by phase plots (Plates 1d and 2d) which show a minimum SSH occurring at  $12^\circ\text{N}$  during January ( $180^\circ$  phase). The NECC at  $6^\circ\text{N}$  also has a maximum in January; that is, its transport variation is in phase with the NEC. As the NEC is the return flow of the subtropical gyre, the similarity between the annual fluctuations in the NEC in the Geosat and model suggests that the wind-forced variability of the North Pacific subtropical gyre is realistically simulated by the model.

Maximum transport of the South Equatorial Current (SEC) occurs at different times at different points along the current. The NEC does not exhibit this behavior because the phase of the SSH to its north does not vary significantly with longitude and similarly with the phase to its south. The phase maps of the annual cycle (Plates 1d and 2d) show a westward propagation of SSH along the equator as a  $-180^\circ$  phase at  $100^\circ\text{W}$ , a phase of  $0^\circ$  near  $180^\circ\text{E}$ , and a slightly positive phase near  $160^\circ\text{E}$ . Thus a SSH high begins near the South American coast in July, reaches  $180^\circ\text{E}$  in January (see the cosine coefficients of Plates 1a and 2a), and reaches New Guinea by April (see the sine coefficients of Plates 1b and 2b). As this propagating SSH high occurs on the north side of the SEC, the annual strengthening/weakening of the SEC propagates westward. Thus the SEC shows a strengthening in March to April (see sine coefficients in Plates 1b and 2b) over the region from  $170^\circ\text{W}$  to  $100^\circ\text{W}$  and a strengthening a few months later over the region from  $140^\circ\text{E}$  to  $180^\circ\text{E}$ . The annual propagation of high SSH is along the south side of the NECC, so the NECC has some of the same propagating strengthening/weakening but not to the extent of the SEC since the NECC is bounded to the north by a region of constant phase.

Another band in the annual amplitudes (Plates 1c and 2c) extends from the east coast of New Guinea southeastward to  $160^\circ\text{W}$ . This is caused by annual variability in the South Equatorial Countercurrent (SECC). The intensification of this current occurs in March to April which corresponds to the time of the sine coefficient (Plates 1b and 2b). The annual variation of the SECC extends from  $7^\circ\text{S}$  at  $160^\circ\text{E}$  to  $13^\circ\text{S}$  at  $160^\circ\text{W}$ , with a high SSH to the north and a low SSH to the south. The model annual amplitude (Plate 2c) shows the SECC at  $5^\circ\text{S}$  extending farther eastward (to  $120^\circ\text{W}$ ) than the Geosat data. This major difference between the annual equatorial variations in the Geosat observations and the model simulation can be seen best in the phase maps of Plates 1d and 2d near the southern boundary from  $140^\circ\text{W}$  to  $80^\circ\text{W}$ . The difference is probably due to the artificial closed boundary in the model at  $20^\circ\text{S}$ .

To better observe latitudinal variations in the annual

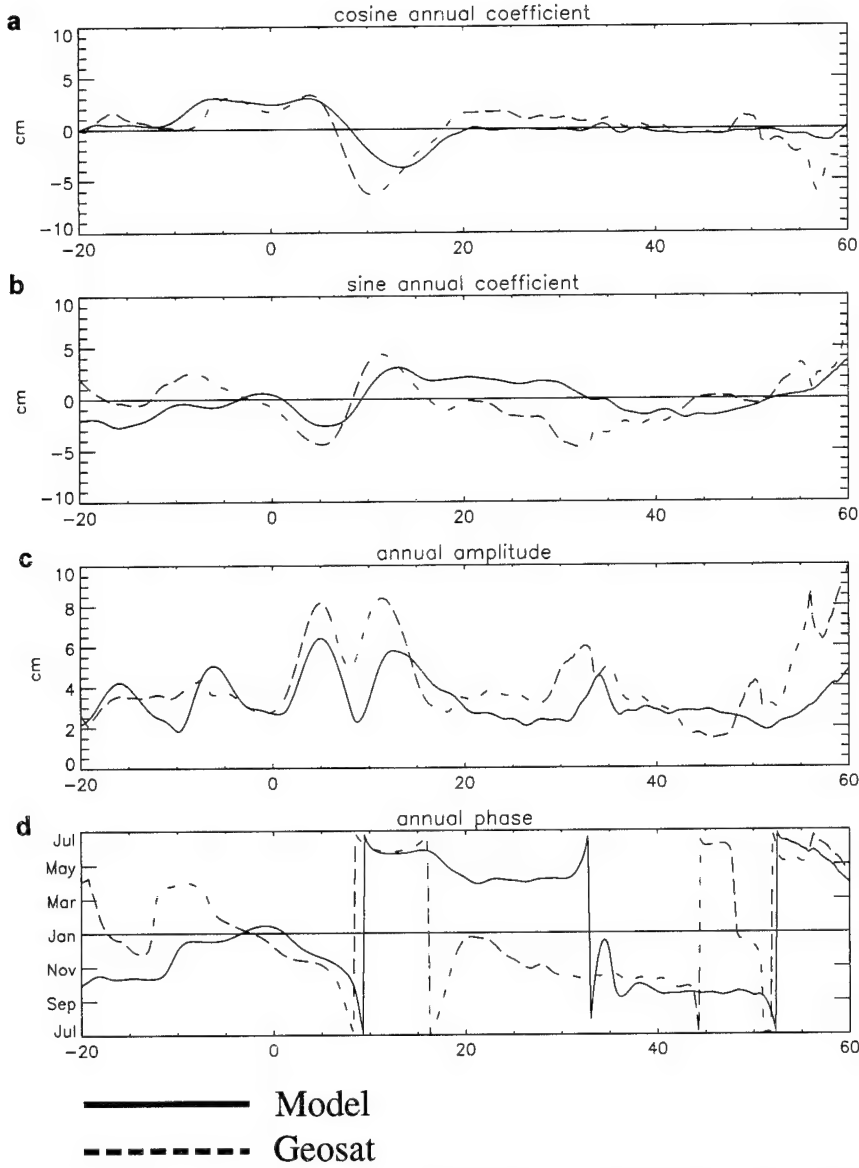


**Figure 3.** (a) Cosine coefficient, (b) sine coefficient, (c) amplitude, and (d) phase computed from the averaged cosine and sine coefficients of the annual cycle averaged at each latitude from  $140^{\circ}$  E to  $100^{\circ}$  W for Geosat (dot-dashed line) and the model (solid line). Figures 3a and 3b are derived from Plates 1a and 2a and Plates 1b and 2b, respectively. Peaks in Figure 3c from  $20^{\circ}$  S to  $20^{\circ}$  N are due to equatorial currents, and the peaks just south of  $35^{\circ}$  N are due to the recirculation gyres just south of the Kuroshio Extension. Geosat indicates amplitudes higher than the model by about 2 to 4 cm which is the Geosat noise floor seen in Figure 2. Good agreement is obtained in Figure 3d between the model and Geosat over the equatorial regions ( $20^{\circ}$  S to  $17^{\circ}$  N), but a large shift in phase occurs over the southern portion of the North Pacific gyre ( $20^{\circ}$  N to  $30^{\circ}$  N) due to steric effects present in the Geosat data but not the model. The model and Geosat again agree north of  $30^{\circ}$ .

signal, a mean of the cosine and sine coefficients is taken from  $140^{\circ}$  E to  $100^{\circ}$  W. The results are plotted in Figures 3a and 3b, with dot-dashed lines indicating Geosat and solid lines indicating the model. The averaged amplitude and phase produced from the averaged sine and cosine functions are plotted in Figures 3c and 3d. The amplitude peaks from the equatorial current systems at  $5^{\circ}$  S,  $5^{\circ}$  N, and  $12^{\circ}$  N are apparent. Another minor peak is evident at  $15^{\circ}$  S. The model peaks in the southern hemisphere are slightly larger than the Geosat peaks due to the model's zonally stretched southern equatorial currents. At most latitudes the Geosat amplitudes are larger than the model amplitudes by 2 to 4 cm, which is the altimeter noise floor seen in the frequency spectra of section 2. The phase of Figure 3d shows

agreement between the model and altimeter data from  $5^{\circ}$  S to  $17^{\circ}$  N, with Geosat slightly leading the model by about 2 weeks. South of  $5^{\circ}$  S, the average model phase is corrupted by the extended model SECC.

As seen in Figure 3d, the region from  $20^{\circ}$  N to  $30^{\circ}$  N is a region of significant difference between the model and altimeter phase. These differences arise because the model is only a hydrodynamic model, implying that the density in each layer is fixed in time and space, and no heat fluxes are input to the model. Because of this, there is no steric effect on the SSH variability of the model, but there is such an effect in the Geosat data. The steric SSH variations are greatest from  $20^{\circ}$  N to  $30^{\circ}$  N in the southern portion of the North Pacific gyre. This effect keeps the phase of the North Pacific gyre

relatively constant from 20°N to 40°N in the Geosat data, but its absence in the model simulation causes a jump in the phase of the model results at 33°N.

The recirculation gyres of the Kuroshio Extension are apparent from 30°N to 35°N as amplitude peaks in Figure 3c. These gyres constitute the northern half of the North Pacific gyre and account for a large portion of the annual variability of the Kuroshio Extension transport [Qiu, 1992]. The gyres are also very apparent in the Geosat annual sine coefficient (Plate 1b) at 150°E and 160°E just south of the Kuroshio Extension at 35°N. These are also the longitudinal positions of the semistationary, northward meanders [Mitchell et al., this issue; Mizuno and White, 1983] which have shown the most pronounced northward meandering in summer months. The annual model and Geosat phase across the Kuroshio Extension and recirculation gyres in Figure 3d match much better than across the thermally driven subtropical gyre. This indicates that the annual variations in the recirculation gyres are wind driven rather than thermally driven. The peak transport of the Kuroshio occurs when the recirculation gyres reach their peak amplitude in late October, and it is during the subsequent winter months that the greatest variability in temperature at the 300-m isobath is observed by Mizuno and White, [1983]. The position along the Kuroshio Extension at which the largest variability occurs is observed to be at these recirculation gyres. North of 50°N, the Geosat data and model show increasing amplitude and comparable phase over the subarctic and Alaskan, gyres with Geosat showing a larger amplitude increase than the model.

The semiannual frequency is more difficult to analyze than the annual frequency because its main effect is to change the shape of annual fluctuations from sinusoidal in time. At first glance the Geosat and model semiannual amplitudes (Plates 3c and 4c) are disappointingly low. Previous studies of only Geosat data have dismissed much of the semiannual variations at midlatitudes as data contamination [Jacobs et al., 1992]. However, the amplitude and phase of Geosat and the model share some remarkable characteristics. The main amplitude peaks of Plates 3c and 4c occur over the equator at 160°W to 120°W, east of New Guinea, and over the Kuroshio Extension. These indicate variations in the SEC, SECC, and Kuroshio Extension transport variations, respectively. The phase (Plates 3d and 4d) shows correlation over very large regions, particularly over the equator, around 40°N, and near the northern limit of the domain.

One striking pattern occurring in both the model and Geosat is a band in the semiannual phase maps (Plates 3d and 4d) from 10°N to 35°N and from 10°S to 20°S. This band, at first, appears to be noise. However, the scales are much larger than the 100-km roll-off length used to interpolate the data, and Geosat and the model have very distinctive features in this region. The band is dominated by westward propagating anomalies.

An indication of the dominant wavelength and propagation direction of this variability is given in Figure 4 which is a zonal average of the wavelength obtained

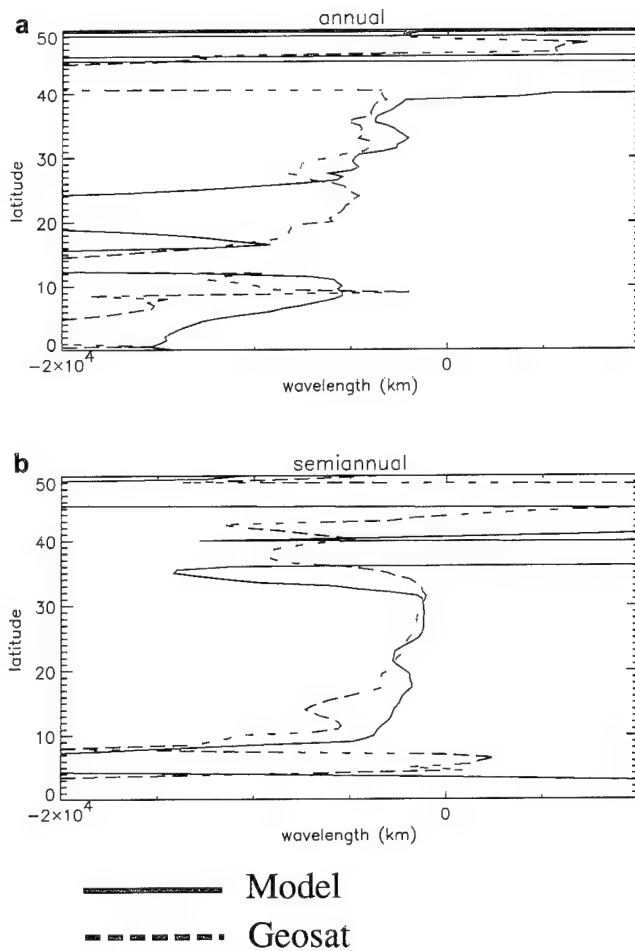
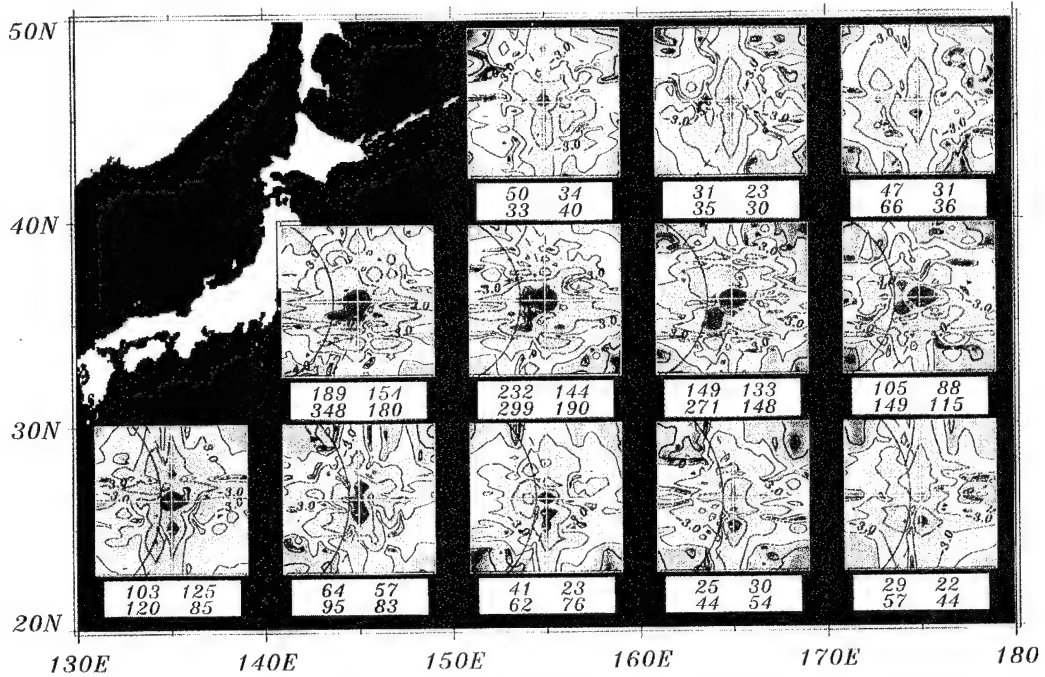


Figure 4. Length of Geosat (solid) and the model (dashed) as a function of latitude at the (a) annual and (b) semiannual frequencies. These were produced from the reciprocal of the mean zonal gradient of the phase of the annual and semiannual frequencies (Plates 1d, 2d, 3d, 4d). Negative wavelengths indicate westward propagation, and positive wavelengths indicate eastward propagation. Very large wavelengths indicate no propagation. The semiannual frequency indicates a band from 10°N to 32°N with characteristic Rossby wave behavior as wavelengths decrease with increasing latitude. The theoretical latitude extent of semiannual Rossby waves is 35°, and 45° is the limit of annual Rossby waves. Both frequencies exhibit radical changes in wavelength at these critical latitudes.

from each frequency. Wavelength is calculated by the reciprocal of the gradient of the phase in the east-west direction. Negative values of wavelength indicate westward propagation, and positive values indicate eastward propagation. The semiannual frequency indicates westward propagating waves, with wavelengths decreasing from about 5000 km at 10°N to 1000 km at 32°N. North of 32°N, the behavior changes dramatically. Wavelengths increase substantially (above 15,000 km), and eastward propagation appears. Very long wavelengths indicate almost no propagating features; only standing waves are present. The characteristics from 10°N to 32°N are due to the domination of Rossby waves in the region which have a theoretical maximum latitude of about 35° at the semiannual frequency. The decreasing wavelength with increasing latitude is also expected from Rossby waves.

The latitudinal variations of the zonal wavelength

*Wave number spectra of the annual signal from Geosat data.*



**Plate 5a.** Amplitude spectra in wavenumber space for the annual signal from Geosat derived by a complex discrete Fourier transform over  $10^6$  square regions of the data in Plates 1a and 1b. The log of the amplitude is plotted with the amplitude in meters. The region of wavenumber space covered is -5 to +5 cycles per 1000 km in both the x (east-west) and y (north-south) wavenumber directions. The lines in the negative x half of the plots are the first mode baroclinic and the barotropic dispersion curves from quasi-geostrophic theory. The four numbers below each spectrum are the total of the amplitude squared in their respective quadrants times 106 and thus are related to total sea surface height propagation in their respective directions. The Geosat spectra show a preference to the southwest at  $35^\circ$  N, while the model spectra (Plate 6a) indicate a northwest preference at  $35^\circ$  N. Averaged over all the spectra, the ratio of westward to eastward propagating SSH for the annual period is 1.33 for Geosat and 1.28 for the model.

*Wave number spectra of the semiannual signal from Geosat data.*

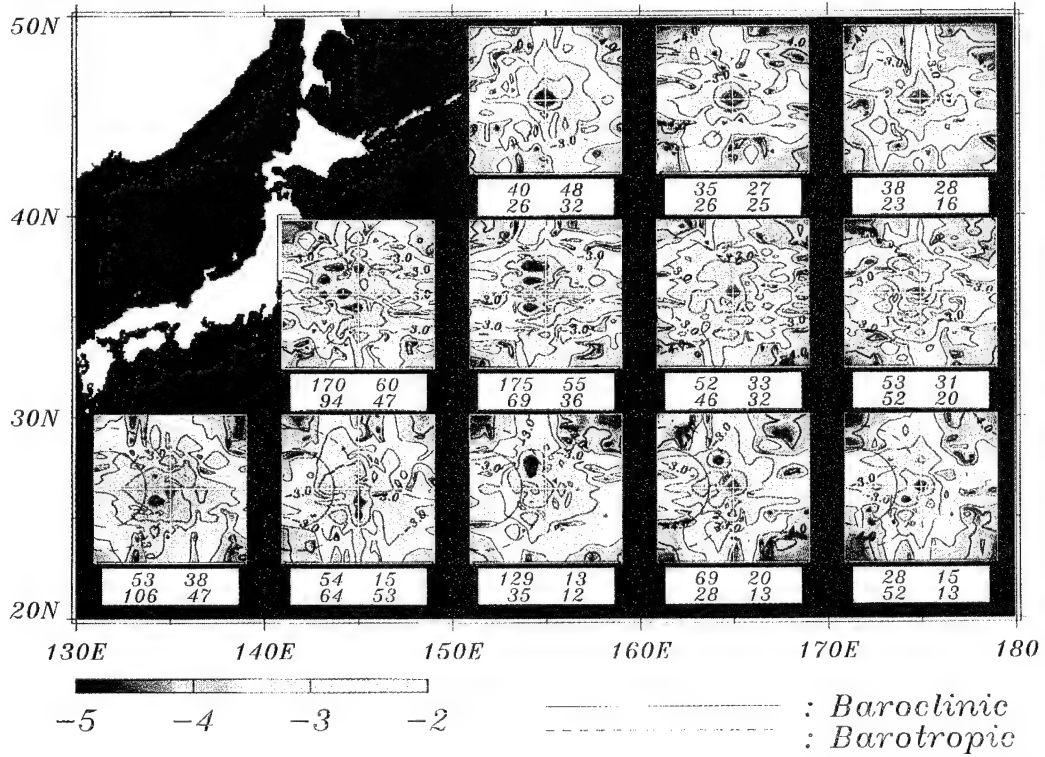


**Plate 5b.** Same as in Plate 5a, but for the semiannual signal from Geosat derived from data in Plates 3a and 3b. Averaged over all the spectra, the ratio of westward to eastward propagating SSH is 2.03 for Geosat and 1.65 for the model at the semiannual period. Averaged over the spectra at  $45^\circ$  N, the west to east propagation ratio is 1.08 for Geosat and 1.06 for the model. Averaged over the spectra at  $25^\circ$  N, the ratios are 2.49 and 3.57 for Geosat and the model, respectively. Semiannual first mode baroclinic Rossby waves have a northern limit of  $35^\circ$  N, so the westward propagation is expected to significantly drop from  $25^\circ$  N to  $45^\circ$  N.

*Wave number spectra of the annual signal from model data.*

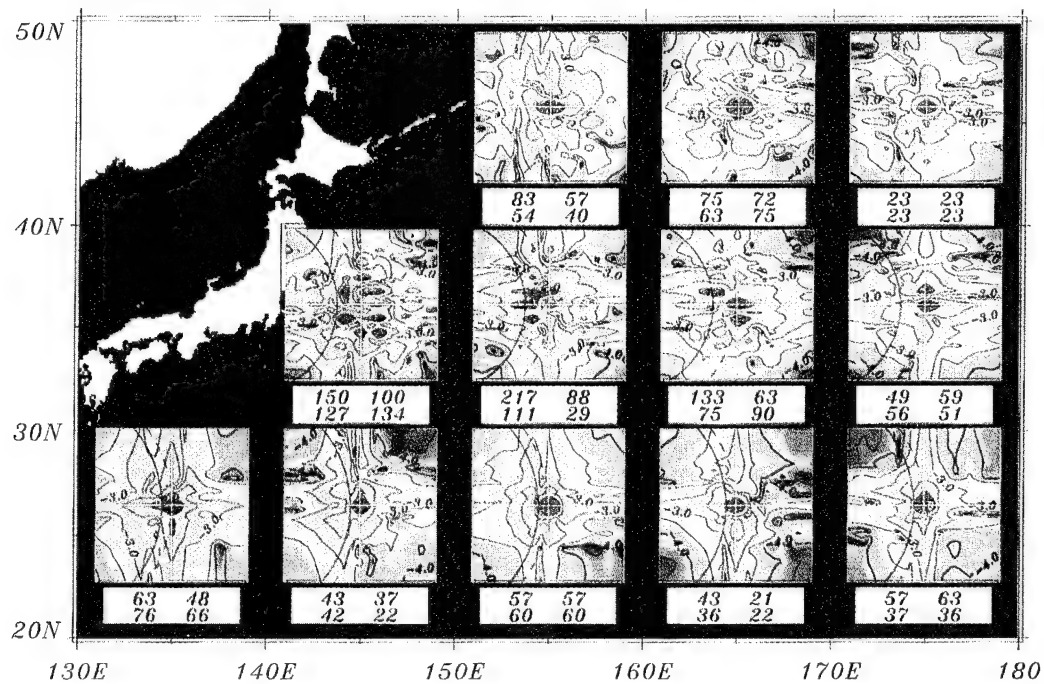


Plate 6a. Same as in Plate 5a, but for the annual signal from the six layer model derived from data in Plates 2a and 2b.

*Wave number spectra of the semiannual signal from model data.*

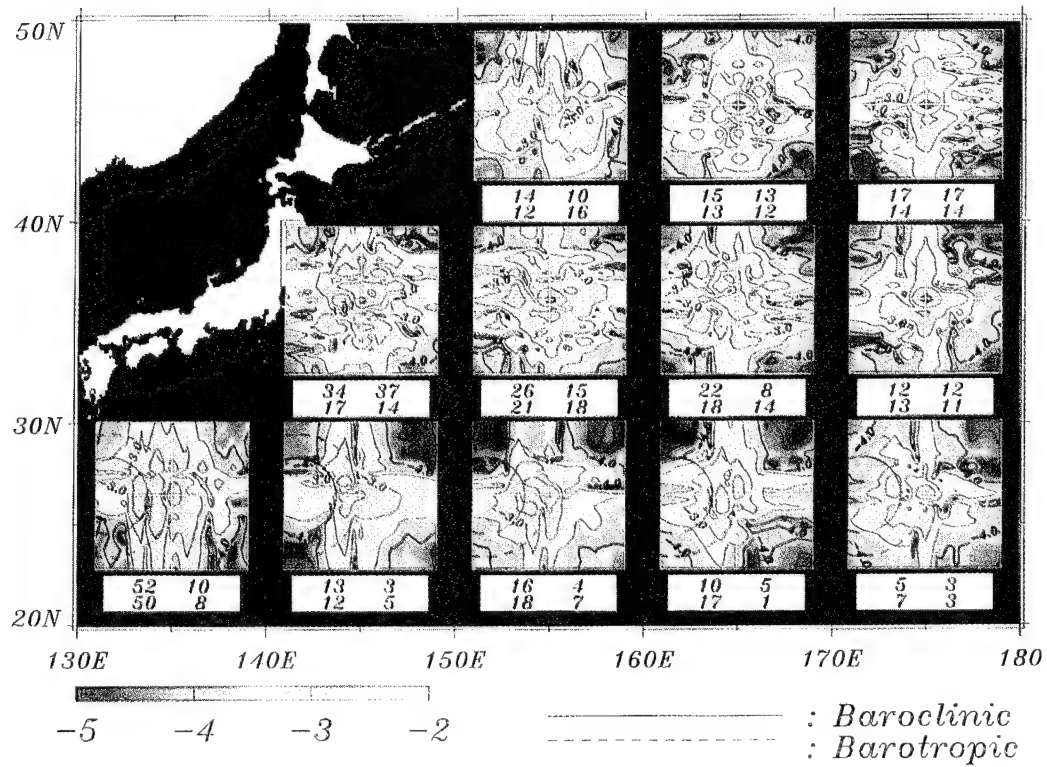


Plate 6b. Same as in Plate 5a, but for the semiannual signal from the six layer model derived from data in Plates 4a and 4b.

and propagation direction of the annual frequency indicate a behavior similar to the semiannual. A zonal band of westward increasing phase exists at the annual frequency in the phase plots (Plates 1d and 2d) from  $10^{\circ}$  to about  $45^{\circ}$ , where  $45^{\circ}$  is the theoretical maximum latitude limit for annual baroclinic Rossby waves. The wavelengths at the annual frequency are longer than the semiannual as would be expected for Rossby waves. The model indicates a zone from  $20^{\circ}$ N to  $25^{\circ}$ N (Figure 4) which contains no propagation as wavelengths become very long. This is in contrast to the Geosat wavelengths which indicate a westward propagation. The intensification of the NEC is present from  $10^{\circ}$ N to  $15^{\circ}$ N as very long wavelengths, again implying that the current strengthens simultaneously at all points along the current. The westward propagating strengthening of the SEC is seen in Figure 4 from  $5^{\circ}$ N to  $10^{\circ}$ N at wavelengths from 5000 to 10,000 km. The annual wavelengths in Figure 4 indicate more noise than the semiannual. This is due to the ratio of Rossby wave to non-Rossby wave activity at the annual cycle being much lower than that of the semiannual. Section 5 shows that the semiannual cycle is dominated by Rossby wave behavior south of  $35^{\circ}$ N.

## 5. Wavenumber Decomposition

To examine the spatial variations in the Kuroshio Extension region, a two-dimensional wavenumber de-

composition of the the SSH anomaly annual and semiannual cycles is performed. The sine and cosine coefficients discussed in section 4 are used in a complex two-dimensional discrete Fourier transform to determine amplitudes in wavenumber space. The discrete Fourier transform used is given by

$$G(\lambda_x, \lambda_y) = \frac{1}{nx ny} \sum_{ix=0}^{nx-1} \sum_{iy=0}^{ny-1} g(ix, iy) e^{i2\pi(\lambda_x ix/nx + \lambda_y iy/ny)} \quad (1)$$

where  $G(\lambda_x, \lambda_y)$  is the transform at the wavenumber  $(\lambda_x, \lambda_y)$  of the complex function  $g(ix, iy)$  which is available at the points  $(ix, iy)$ ;  $nx$  and  $ny$  are the number of points in the  $x$  (longitudinal) and  $y$  (latitudinal) directions, respectively. This decomposition is conducted over  $10^{\circ}$  squares to observe changing spatial dynamics over the region as discussed in section 1. The amplitudes are contoured in wavenumber space for each frequency and for each data set. The resulting amplitude spectra in wavenumber space are presented in Plates 5a and 5b for the Geosat data and Plates 6a and 6b for the six-layer model. The circular curves drawn in Plates 5 and 6 are the Rossby wave dispersion relations for the barotropic and first baroclinic modes. These curves are based on a longitudinally averaged Rossby radius as determined by *Emery et al.* [1984]. Wavenumbers in the  $x$  and  $y$  directions vary from -5 to 5 cycles per

### Ratio of amplitude spectra (Geosat/Model) for the annual cycle.

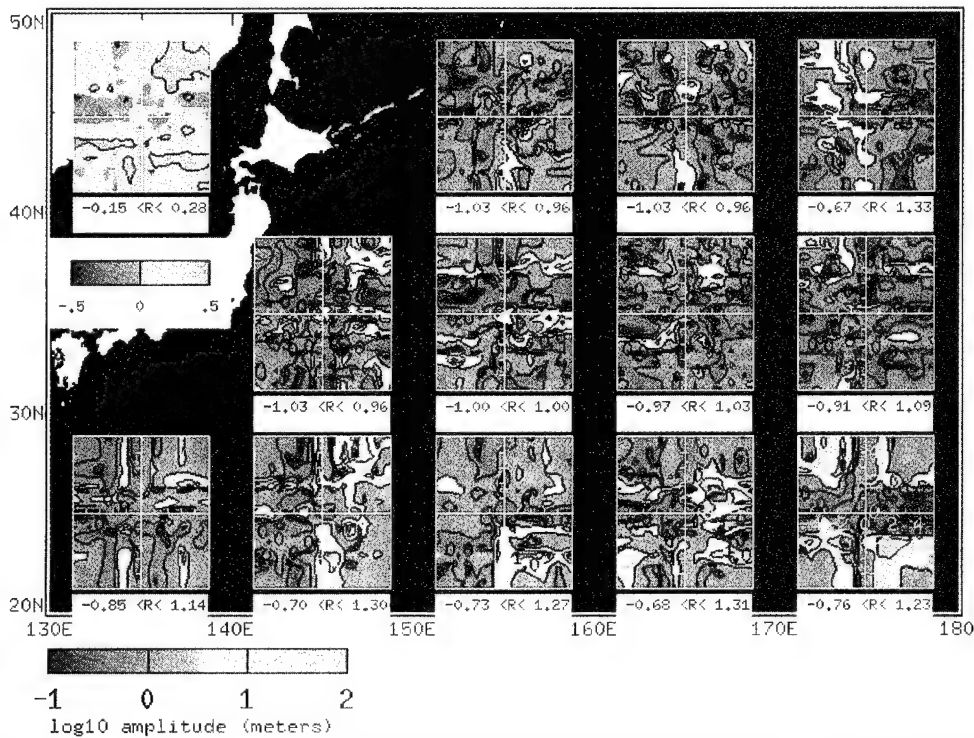


Plate 7. Ratio of the amplitude spectra (Geosat/model) of the annual signal in Plates 5a and 6a. The log of this ratio is plotted, so equal amplitudes are indicated by a value of 0. Intervals under each plot are the range of the ratio that does not indicate a significant difference between model and Geosat spectra. Values lying outside this interval are significantly different at a 98% confidence level. The spectrum in the top left corner is the ratio of the averaged Geosat spectrum to the averaged model spectrum. Contours on this spectrum are at the interval range endpoints.

Ratio of amplitude spectra (Geosat/Model)  
for the semiannual cycle.

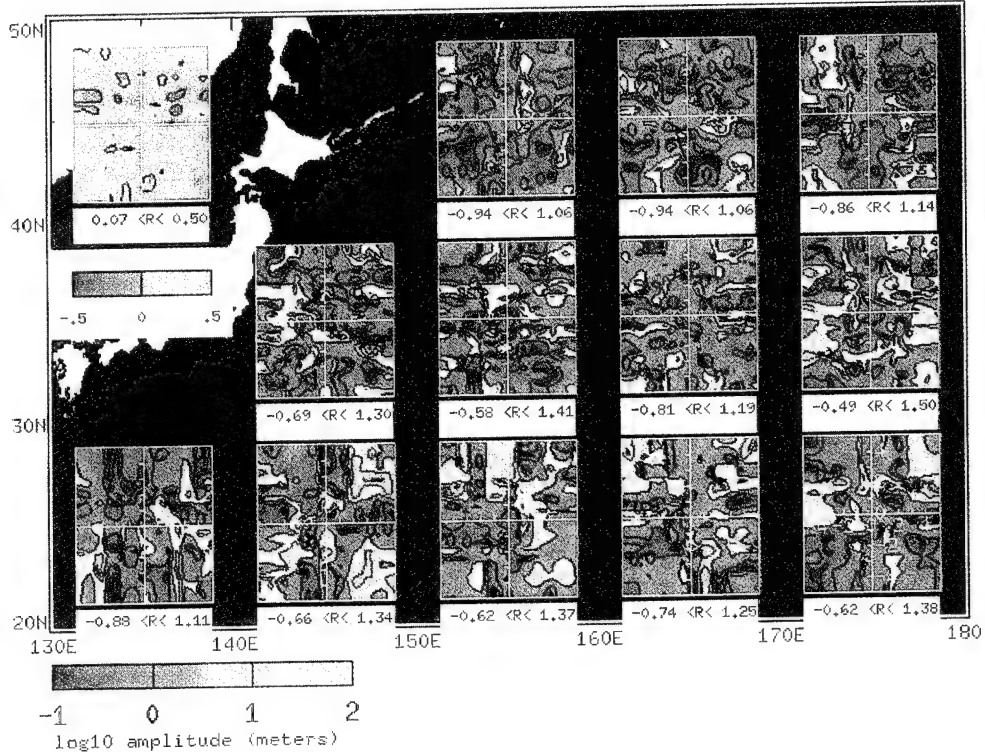


Plate 8. Same as in Plate 7, but for the semiannual signal in Plates 5b and 6b.

1000 km. The four numbers below each spectral plot indicate the magnitude of the energy of SSH variability which is propagating to the northwest (top left number), southwest (bottom left number), northeast (top right number), and southeast (bottom right number). Each number is the sum of the squared amplitude over one quadrant of wavenumber space, then multiplied by  $10^7$ . None of the amplitudes on the  $x = 0$  or  $y = 0$  wavenumber axis is included in these numbers.

### 5.1. Standing and Propagating Waves

The amplitude spectra indicate the spatial structure of variations at the annual and semiannual frequencies. All the information and processes seen in the annual and semiannual frequencies (Plates 1-4) are contained within the spectra. The spectra present a second method of viewing the information at each frequency. It is useful to first recognize some of the major signals apparent in the annual and semiannual amplitude and phase maps. This aids in understanding the spectra and determining what new information is available in the spectra which could not easily obtain directly from Plates 1-4.

The amplitude at the origin of the spectra is not the average of the amplitude from Plates 1-4 over the  $10^\circ$  squares, but it is the amplitude obtained from the average cosine and average sine coefficients over the  $10^\circ$  region. Thus the SSH variability on scales larger than

the  $10^\circ$  square contributes to the amplitude at the origin.

The annual variations in the Kuroshio Extension appear mainly as changes in transport strength through the recirculation gyres. The annual Geosat sine coefficient (Plate 1b) indicates this recirculation as a negative region south of the Kuroshio Extension. The negative value of this region implies that the recirculation gyre is weakest during the spring and strongest in the fall. The spatial structure of the recirculation gyre is mainly a function of latitude, with some variation in longitude. The annual variations of this spatial function create a standing wave. The transform of a function which varies only with latitude produces a spectra with energy only at  $x$  wavenumber 0. Additionally, since the spatial function appears as a standing wave, the transform is symmetric about the origin. Many of the spectra indicate energy at  $x$  wavenumber 0 which is symmetric about the origin. Thus a large amount of the variability at each frequency appears as a standing wave, with the amplitude being a function of latitude. Other effects such as steric anomaly are functions mainly of latitude, but the effects are not standing waves. This creates some of the nonsymmetry seen at  $x$  wavenumber 0.

The longitudinal variations of the recirculation gyre south of the Kuroshio Extension produce bands at constant  $y$  wavenumbers. Again, the standing wave structure forces the spectra to be symmetric about the origin. This produces bands in many spectra at  $y$  wavenumbers

at  $+\/- 1$  and  $+\/- 2$ . These bands are most evident directly over the Kuroshio Extension at  $35^{\circ}\text{N}$ .

By examining the spectra, additional information is gained from the energy which lies off the axis and is not symmetric about the origin. The spectra reveal the direction and wavelength of propagating features at each frequency. Peaks in the amplitude spectra correspond to plane waves propagating in the direction of a vector drawn from the origin to the peak with a wavelength inversely proportional to the distance of the peak from the origin. These propagating versus standing waves are not as evident in the amplitude and phase plots (Plates 1-4).

By comparing the magnitudes of the four numbers beneath each spectra, an indication is given of the relative dominance of each direction of propagation over each region. For example, certain areas indicate more warm core eddy sheddings by a dominance of northwestward propagation, while other areas indicate more cold core eddies by a dominance of southwestward propagation. An indication of the dominant length scale is given by the distance from the origin of wavenumber space to the peak amplitudes. The farther the peak amplitudes are from the origin, the shorter are the dominant length scales.

## 5.2. Annual Results

The wavenumber spectra are very useful for dividing the Kuroshio Extension into different dynamical regions. From the annual spectra (Plates 5a and 6a) there is a difference between the northern and southern sides of the Kuroshio Extension (the spectra at  $45^{\circ}\text{N}$ ), the Geosat and model annual spectra exhibit a distinct northwestward preference for SSH propagation at  $155^{\circ}\text{E}$  indicated by the generally higher amplitudes in the top left quadrant of the spectra and the relatively large magnitude of the energy number for this quadrant below the spectrum. Farther to the east, Geosat's preference of propagation turns to the southwest.

In the Kuroshio Extension (at  $35^{\circ}\text{N}$ ), amplitudes are much higher than in other regions due to the strong meandering and eddy shedding of the current, and westward propagating SSH anomalies dominate eastward propagation (Plates 5a and 6a). In the Geosat data the southwestward direction is preferred over northwestward along the entire Kuroshio Extension axis. The model indicates a preference to the northwestward direction out to  $170^{\circ}\text{E}$ . From  $165^{\circ}\text{E}$  to  $175^{\circ}\text{E}$  there is a decrease in SSH variability energy as the Kuroshio Extension crosses the Emperor Seamounts at  $170^{\circ}\text{E}$ . The bias toward a preferred direction of propagation decreases in both data sets east of the seamount chain.

At the band centered at  $25^{\circ}\text{N}$  the Geosat data indicate a stronger southward propagation than the model. There are bands at  $y$  wavenumber -2 and -3 which do not appear in the model spectra. These are associated with the variations in the steric anomaly.

The westernmost spectra at all latitudes generally indicate more eastward propagation than other spectra

at their latitude. Reflected waves and other boundary processes are probable sources of this eastward propagation in SSH variability energy. Eddies also have been observed to propagate eastward as they are reabsorbed into Kuroshio Extension in the western boundary regions [Ichikawa and Imaizumi, 1994].

In addition to the change in propagation direction over the region, the wavelength (which is inversely proportional to the distance between a peak in wavenumber space and the origin) varies with latitude. In the southern band at  $25^{\circ}\text{N}$  (Plates 5a and 6a) the dominant wavelengths are much larger than at the northern latitudes. This is indicated by amplitude peaks in the spectra extending farther into the negative half of wavenumber space at  $35^{\circ}\text{N}$  than at  $25^{\circ}\text{N}$ . The change toward smaller wavelengths with increasing latitude is in agreement with the change in the baroclinic Rossby wave dispersion curve. The theoretical curve for unforced baroclinic Rossby waves is a circle with a radius which decreases with increasing latitude. At about  $45^{\circ}\text{N}$  the radius becomes 0, and annual Rossby waves cannot exist above this latitude limit. Over most regions the peaks falling near the baroclinic dispersion curves tend to be shifted slightly toward the origin. That is, wavelengths implied by the model and Geosat spectra are longer than those dictated by the theoretical curves. In the Kuroshio Extension region the ratio of westward to eastward propagating SSH energy for the annual period is 1.33 for Geosat and 1.28 for the model as determined from the sum of the amplitude-squared numbers for each spectrum given in Plates 5a and 6a.

## 5.3. Semiannual Results

The spectra of semiannual variability from Geosat and the model data (Plates 5b and 6b) indicate a larger fraction of SSH variability with westward propagation than do the annual spectra. At the semiannual frequency the ratio of westward to eastward propagating SSH variability averaged over the entire region is 2.03 for Geosat and 1.65 for the model. At the northern latitude of  $45^{\circ}\text{N}$  there is no significant predominance of westward over eastward propagation in either Geosat or the model as seen in the quadrant numbers below each spectrum. The ratio of westward to eastward propagating SSH anomalies at the semiannual frequency at  $45^{\circ}\text{N}$  is 1.08 for Geosat and 1.06 for the model. At  $25^{\circ}\text{N}$  the ratios are 2.49 and 3.57 for Geosat and the model, respectively. Semiannual baroclinic Rossby waves have a northern limit of  $35^{\circ}\text{N}$ , so it is not surprising that westward propagation significantly drops from  $35^{\circ}\text{N}$  to  $45^{\circ}\text{N}$ .

There is an increase in eastward propagation at the western boundary at this frequency, just as in the annual variability. In the Kuroshio Extension from  $140^{\circ}\text{E}$  to  $160^{\circ}\text{E}$  the Geosat spectra (Plate 5b) show a preference toward northwestward propagation which is opposite to the preference in the annual Geosat spectra (Plate 5a). Model spectra at the semiannual frequency over the region (Plate 6b) show the same northwest preference as the annual spectra (Plate 6a).

Over the southern band at 25°N the Geosat data manifest much higher peaks than the model. In this southern band, both the model and Geosat show extreme prejudice toward westward propagation. The phase of the semiannual cycle for both the model (Plate 4d) and Geosat (Plate 3d) at first appeared to be largely noise contamination or random processes. However, the spectra indicate that the majority of the variability is westward propagation. The variation of the wavelength with latitude (Figure 4) indicates that the wavelength decreases with increasing latitude as expected from the simple linear Rossby wave theory. This is again evidenced by the lack of any preference of westward over eastward propagation at 45°N compared with the dominant westward propagation at 25°N.

#### 5.4. Comparison of Amplitude Spectra

To facilitate further comparison of Geosat and model spectra, the ratio of the amplitude spectra are plotted in Plates 7 and 8. The ratio range shown under each plot gives an interval which indicates where the spectra are not significantly different at a 98% confidence level. The amplitude squared at each point in wavenumber space is a chi-square variable with 2 degrees of freedom, and the ratio of two chi-square variables is an *F*-distributed variable with 2 and 2 degrees of freedom. Thus the confidence intervals shown for the ratio of the squared amplitudes are computed from

$$\log \sqrt{\frac{\sigma_g^2}{\sigma_m^2 F_{.99}(2,2)}} \leq \log \sqrt{\frac{G_g G_g^*}{G_m G_m^*}} \leq \log \sqrt{\frac{\sigma_g^2}{\sigma_m^2 F_{.01}(2,2)}} \quad (2)$$

where  $\sigma_g^2$  and  $\sigma_m^2$  are the variance of the particular frequency of Geosat and model data, respectively, over the 10° region;  $G_g$  and  $G_m$  are the discrete Fourier transforms for Geosat and model, respectively; and the asterisk signifies a complex conjugate. The ratio of the average squared amplitude spectra for each frequency is shown in the top left corners of Plates 7 and 8. That is, the spectra for Geosat and the model are averaged over the northwest Pacific region (over all 12 of the 10° boxes), and then the ratio of the average spectra is computed. The number of degrees of freedom changes from 2 at each point in wavenumber space to 24 (given 12 estimates of the spectra and assuming that the data in each 10° square are independent). Note that the confidence interval for the ratio  $R$  on these plots is much smaller due to the larger number of degrees of freedom. This makes detecting differences much easier. A different scale range is used for the average plots so that these smaller differences may be more easily seen. Contours are drawn on the ratio of the average spectra at the confidence interval endpoints noted underneath the plot. The ratio of the amplitude spectra shows which data set contains more SSH variability and at what wavenumber the variability is predominant. The log of the ratio is plotted, so values of 0 indicate equal values in both Geosat and model amplitudes.

At the annual frequency in Plate 7 the ratio of the wavenumber spectra at the origin is generally near 0 which indicates that the gyre-scale fluctuations are equivalent in the two data sets. Larger ratios of the annual frequency spectra are seen at larger wavenumbers, indicating a greater similarity between Geosat data and the model at longer scales. Differences at the smaller scales can be explained by a variety of processes. In addition to subgrid-scale physics and timescales less than a few hours being excluded from the model, eddy viscosity in the model is unrealistically high. The viscosity cannot be significantly lowered without increasing horizontal grid resolution, and this high viscosity does reduce variations on shorter scales. White noise in the Geosat data contributes to greater differences at the shorter length scales as white noise is fairly uniform at all wavenumbers and the ocean signal is smaller at short length scales than at large scales. Thus the ratio of the Geosat signal plus noise to the model signal is larger at the higher wavenumbers.

Mesoscale events are nonlinear and chaotic with respect to the large-scale winds, while the large-scale gyre circulations are deterministic with respect to this large-scale forcing. Thus, given a realistic model and accurate wind forcings, it is expected that the model and Geosat spectra will match well on the large scale even though a data set is not sufficiently long to produce a statistically accurate spectra. However, an insufficient sampling of mesoscale events leads to larger dissimilarities at smaller scales. These mesoscale events are not as dependent on the wind forcing as is the gyre-scale circulation. Thus at higher wavenumbers the spectra presented here are easily influenced by isolated mesoscale events in either the model or the Geosat data. Real ocean processes present in the Geosat data can also produce significant differences. Small time- and space-scale effects such as gravity waves have been removed from the model results by numerical filtering procedures and exclusion of various dynamics from the model. The steric anomaly prevalent over the southern half of the north Pacific gyre causes larger differences in the southern bands than in the northern bands. At 45°N the spectra are very similar where steric effects are not large.

The ratios of the wavenumber spectra at the semiannual period in Plate 8 show larger model-Geosat differences than those at the annual period, with the model manifesting smaller amplitudes than the Geosat data. This is probably due, in part, to white noise in Geosat which can produce the same effect in frequency as is described above in wavenumber since the semiannual frequency contains less variability than the annual. However, as shown by Hurlburt *et al.* [this issue], part of the difference between the model and Geosat is due to a need for even higher horizontal resolution in the numerical model.

The average ratios shown in the top left corner of Plates 7 and 8 generally have values within the confidence intervals (i.e., good Geosat/model spectra comparison). At the annual frequency (Plate 7) the average spectra indicate Geosat having higher amplitudes

than the model except for northwestward propagating SSH. From the individual annual spectra in the Kuroshio Extension, Geosat has a southwestward preference, while the model has both northwestward and southwestward propagation preference. Significant differences occur in the average spectra ratio at wavenumber (3,3). This probably arises from the region centered at 35°N, 145°E. Over this region, Mizuno and White [1983] observed several eddies propagating northeastward in their 4-year time series. Hence such differences could be due to limitations of the relatively short time series of data (3 years) which is not long enough to permit observation of a large number of ring separation events. Geosat also shows significantly more variability over a band at  $y$  wavenumber -3. This can be seen along 25°N in the individual spectra ratios from 150°E to 180°E at 25°N in Plate 6. It is over this region that steric effects in Geosat produce large differences. This effect is evident in the phase of the annual cycle of Figure 3d.

The average ratio of the semiannual period shown in Plate 8 indicates that Geosat has more variability than the model as is the case with the annual variability. The most significant average difference in the semiannual signal occurs at a  $y$  wavenumber of +2. In the individual spectra ratios the majority of this higher variability is coming from the steric region from 150°E to 180°E along 25°N.

## 6. Conclusions

SSH variability from the Geosat altimeter and a 1/8°, six-layer primitive equation model of the North Pacific Ocean is compared in frequency-wavenumber space. Annual and semiannual frequencies dominate in both the Geosat and the model variability. The timing of seasonal variations is similar in both data sets as evidenced by the agreement in phase. Major wind-forced features such as the equatorial currents and Kuroshio Extension indicate equivalent amplitudes and phases in both data sets.

New results indicate that the annual variations in the South Equatorial Current propagate westward and require 9 months to cross the Pacific basin. The North Equatorial Current does not indicate such a propagating characteristic. The NEC strengthens and weakens as a whole across the Pacific basin; there is no phase variation along the NEC at the annual frequency. The variations in the Kuroshio Extension transport are seen mainly in the recirculation gyres just south of the extension. The maximum Kuroshio Extension transport occurs in October in both the model and Geosat data. As the model is driven by wind forcing and no thermal forcing, the recirculation gyres are mainly a wind-forced feature.

The major area of disagreement between the model and Geosat data is from about 25°N to 30°N. Over this region the annual variations of the model and Geosat are about 180° out of phase. The disagreement occurs due to the model being forced by only winds and no

thermal fluxes. Thus the seasonal steric heating and cooling has a major impact on this region, dominates over wind-forced variations, and is 180° out of phase from the wind-forced circulation.

Wavenumber decomposition at the two major frequencies suggests similar dynamics in the two data sets, particularly at large wavelengths and longer timescales. Differences at shorter timescales and wavelengths are partially due to noise and unmodeled processes in the Geosat data. Also, stochastic mesoscale features are not adequately sampled for statistical comparisons over a 3-year time series.

At the annual and semiannual periods both data sets are roughly consistent with linear Rossby wave theory. A majority of SSH variability is evident as westward propagating features, and the features decrease in wavelength with increasing latitude. Rossby wave characteristics also are apparent in the annual and semiannual phase plots as decreasing wavelength with increasing latitude (Figure 4). Abrupt changes in the wavelength characteristics are seen at the critical latitude of both the annual (45°N) and semiannual (35°N) frequencies.

The semiannual frequency is found to be dominated by Rossby waves below 35°N. The semiannual amplitudes of both the Geosat and model (Plates 3c and 4c), at first examination, are disappointingly low and the phase (Plates 3d and 4d) appears to be noise. Previous work had dismissed much of the signal in the Geosat semiannual phase as data contamination [Jacobs et al., 1992]. However, the model and Geosat share very distinctive characteristics in the variations of wavelength with latitude (Figure 4). Westward propagating SSH anomalies are seen to dominate below the critical semiannual Rossby wave latitude (Plates 5b and 6b), and there is no preference for eastward or westward propagation above the critical latitude.

Of course, not all of the energy lying near the dispersion curves is due to Rossby wave propagation but is also due to events such as eddies shed by the Kuroshio which have dynamical balances very similar to Rossby waves. Observed spectral amplitudes do not exactly follow the Rossby dispersion curves for a variety of reasons: forcings of the events are not accounted for in the theoretical curves; the discretization of wavenumber space is about 1 cycle per 1000 km, so points of the discrete Fourier decomposition will probably not fall exactly on the dispersion curves; and the theoretical dispersion curves do not include some dynamical characteristics of the ocean which the model does (mean vertical shear effects, bottom topography, etc.). Generally, the energy in the spectra is constrained to wavelengths slightly longer than the dispersion relation. This implies that phase speeds in the model and Geosat data are higher than those predicted by simple quasi-geostrophic theory and the Rossby radii by Emery et al. [1984].

The generally good correlation between model and altimeter SSH variations observed here encourages use of the model to better understand the altimeter data in future studies. Oceanographic signals present in the altimeter which is partially obscured by noise or other

processes may be better understood by first demonstrating their similarity to the model and then using the model to more completely analyze the underlying dynamics. Vertical variations may also be explored from model output where only the surface expressions are available from the altimeter data.

**Acknowledgments.** This work is a contribution to the Kuroshio Regional Experiment (KERE) and the Eddy-Resolving Global Ocean Modeling project, both sponsored by the Office of Naval Research under program element 61153N. This document, NRL contribution NRL/JA/7327-93-0019, has been reviewed and is approved for public release.

## References

- Carnes, M. R., and J. L. Mitchell, Synthetic temperature profiles from Geosat altimetry: Comparison with air dropped expendable bathythermograph profiles, *J. Geophys. Res.*, 95, 17,979-17,992, 1990.
- Carnes, M. R., W. J. Teague, and J. L. Mitchell, Inference of subsurface thermohaline structure from fields measurable by satellite, *J. Atmos. Oceanic Technol.*, 11, 551-566, 1994.
- Cartwright, D. E., and R. D. Ray, Oceanic tides from Geosat altimetry, *J. Geophys. Res.*, 95, 3069-3090, 1990.
- Chelton, D. B., M. G. Schlax, L. L. Witter, and J. G. Richman, Geosat altimeter observations of the surface circulation of the southern ocean, *J. Geophys. Res.*, 95, 17,877-17,904, 1990.
- Cheney, R. E., B. C. Douglas, R. W. Agreen, L. Miller, D. L. Porter, and N. S. Doyle, Geosat altimeter geophysical data record user handbook, *Tech. Memo. NOS NGS-46*, 32 pp., Natl. Oceanic and Atmos. Admin., Silver Spring, Md., July 1987.
- Egbert, G. D., A. F. Bennett, and M. G. G. Foreman, TOPEX/POSEIDON tides estimated using a global inverse model, *J. Geophys. Res.*, 99, 24,821-24,852, 1994.
- Emery, W. J., W. G. Lee, and L. Magaard, Geographic and seasonal distributions of Brunt-Vaisala frequency and Rossby radii in the North Pacific and North Atlantic, *J. Phys. Oceanogr.*, 14, 294-317, 1984.
- Emery, W. J., G. H. Born, D. G. Baldwin, and C. L. Norris, Satellite-derived water vapor corrections for Geosat altimetry, *J. Geophys. Res.*, 95, 2953-2964, 1990.
- Haines, B. J., G. H. Born, G. W. Rosborough, and J. G. Marsh, Precise orbit computation for the Geosat Exact Repeat Mission, *J. Geophys. Res.*, 95, 2871-2886, 1990.
- Hall, M.M., Energetics of the Kuroshio Extension at 35N, 152E, *J. Phys. Oceanogr.*, 21, 958-975, 1991.
- Hellerman, S., and M. Rosenstein, Normal monthly wind stress over the world ocean with error estimates, *J. Phys. Oceanogr.*, 13, 1093-1104, 1983.
- Hurlburt, H. E., Dynamic transfer of simulated altimeter data into subsurface information by a numerical ocean model, *J. Geophys. Res.*, 91, 2372-2400, 1986.
- Hurlburt, H. E., and J. D. Thompson, A numerical study of Loop Current intrusions and eddy sheddings, *J. Phys. Oceanogr.*, 10, 1611-1651, 1980.
- Hurlburt, H. E., D. N. Fox, and E. J. Metzger, Statistical inference of weakly correlated subthermocline fields from satellite altimeter data, *J. Geophys. Res.*, 95, 11,375-11,409, 1990.
- Hurlburt, H.E., A. J. Wallcraft, W. J. Schmitz, Jr., P. J. Hogan, and E. J. Metzger, Dynamics of the Kuroshio/Oyashio current system using eddy-resolving models of the North Pacific Ocean, *J. Geophys. Res.*, this issue.
- Ichikawa, K., and S. Imawaki, Life history of a cyclonic ring detached from the Kuroshio Extension as seen by the Geosat altimeter, *J. Geophys. Res.*, 99, 15,953-15,966, 1994.
- Jacobs, G. A., G. H. Born, M. E. Parke, and P. C. Allen, The global structure of the annual and semiannual sea surface height variability from Geosat altimeter data, *J. Geophys. Res.*, 97, 17,813-17828, 1992.
- Mitchell, J. L., W. J. Teague, G. A. Jacobs, and H. E. Hurlburt, Kuroshio Extension dynamics from satellite altimetry and a model simulation, *J. Geophys. Res.*, this issue.
- Mizuno, K., and W. B. White, Annual and interannual variability in the Kuroshio Current System, *J. Phys. Oceanogr.*, 13, 1847-1867, 1983.
- National Oceanic and Atmospheric Administration (NOAA) ETOP05 digital relief of the surface of the earth *Data Announce. 86-MGG-07*, Natl. Geophys. Data Cent., Washington, D.C., 1986.
- Qui, B., K. A. Kelly, and T. M. Joyce, Mean flow and variability in the Kuroshio Extension from Geosat altimetry data, *J. Geophys. Res.*, 96, 18,491-18,507, 1991.
- Qiu, B., Recirculation and seasonal change of the Kuroshio from altimetry observations, *J. Geophys. Res.*, 97, 17,801-17812, 1992.
- Schlax, M. G., and D. B. Chelton, Detecting aliased tidal errors in altimeter height measurements, *J. Geophys. Res.*, 99, 12,603-12,612, 1994.
- Schwiderski, E. W., Ocean tides, I, Global ocean tidal equations, *Mar. Geod.*, 3, 161-217, 1980a.
- Schwiderski, E. W., Ocean tides, II, A hydrodynamic interpolation model, *Mar. Geod.*, 3, 219-255, 1980b.
- Tai, C. K., Accuracy assessment of widely used orbit error approximations in satellite altimetry, *J. Atmos. Oceanic Technol.*, 6(1), 147-150, 1989.
- Vazquez, J., V. Zlotnicki, and L. Fu, Sea level variabilities in the Gulf Stream between Cape Hatteras and 50°W: A Geosat study, *J. Geophys. Res.*, 95, 17,957-17,964, 1990.
- Wallcraft, A. J., The Navy Layered Ocean Model user's guide, *NOARL Rep. 35*, 21 pp., Nav. Oceanogr. and Atmos. Res. Lab., Stennis Space Center, Miss., 1991.
- Zlotnicki, V., Sea level differences across the Gulf Stream and Kuroshio Extension, *J. Phys. Oceanogr.*, 91, 599-609, 1991.
- Zlotnicki, V., L.-L. Fu, and W. Patzert, Seasonal variability in global sea level observed with Geosat altimetry, *J. Geophys. Res.*, 94, 17,959-17,969, 1989.
- H. E. Hurlburt, G. A. Jacobs, J. L. Mitchell, and W. J. Teague, Naval Research Laboratory, Code 7323, Stennis Space Center, MS 39529-5004. (e-mail: jacobs@nrlssc.navy.mil)

(Received February 15, 1994; revised July 5, 1995; accepted July 5, 1995.)

# REPORT DOCUMENTATION PAGE

Form Approved  
OMB No. 0704-0188

Public reporting burden for this collection of information is estimated to average 1 hour per response, including the time for reviewing instructions, searching existing data sources, gathering and maintaining the data needed, and completing and reviewing the collection of information. Send comments regarding this burden or any other aspect of this collection of information, including suggestions for reducing this burden, to Washington Headquarters Services, Directorate for Information Operations and Reports, 1215 Jefferson Davis Highway, Suite 1204, Arlington, VA 22202-4302, and to the Office of Management and Budget, Paperwork Reduction Project (0704-0188), Washington, DC 20503.

1. AGENCY USE ONLY (Leave blank)			2. REPORT DATE January 1996	3. REPORT TYPE AND DATES COVERED Journal Article
4. TITLE AND SUBTITLE  An Examination of the North Pacific Ocean in the Spectral Domain using Geosat Altimeter Data and a Numerical Ocean Model			5. FUNDING NUMBERS  Job Order No. 73505603 Program Element No. 0601153N	
6. AUTHOR(S)  G. A. Jacobs, W. J. Teague, J. L. Mitchell <sup>1</sup> , H. E. Hurlburt			Project No. 3208 Task No. 3A0 Accession No. DN259125	
7. PERFORMING ORGANIZATION NAME(S) AND ADDRESS(ES)  Naval Research Laboratory Oceanography Division Stennis Space Center, MS 39529-5004			8. PERFORMING ORGANIZATION REPORT NUMBER  NRL/JA/7323--93-0019	
9. SPONSORING/MONITORING AGENCY NAME(S) AND ADDRESS(ES)  Naval Research Laboratory Systems, Support, and Requirements Stennis Space Center, MS 39529-5004			10. SPONSORING/MONITORING AGENCY REPORT NUMBER	
11. SUPPLEMENTARY NOTES  JOURNAL OF GEOPHYSICAL RESEARCH, VOL. 101, NO. C1, PAGES 1025-1044 <sup>1</sup> Colorado Center for Astrodynamics Research, University of Colorado, Boulder				
12a. DISTRIBUTION/AVAILABILITY STATEMENT  Approved for public release; distribution is unlimited.			12b. DISTRIBUTION CODE	
13. ABSTRACT (Maximum 200 words)  The sea surface height (SSH) variations of the North Pacific ocean and the Kuroshio Extension region, in particular, are examined by frequency and wavenumber decompositions of a 1/8°, six-layer primitive equation Pacific Ocean model and of the Geosat Exact Repeat Mission (ERM) data. Both data sets exhibit peaks in variability at 1 and 2 cycles per year over much of the Kuroshio Extension region. This study is restricted to these two frequencies. Annual variations of equatorial currents in both data sets are similar in both space and time, with the variations in the South Equatorial Current appearing as annual westward propagations. Annual variations in the strength of the Kuroshio Extension are manifested mainly through changes in the strength of the recirculation gyres on the southern side of the current. Annual transport maxima for the Kuroshio Extension occur around late October for both the model and Geosat. Large-scale variations (length scales greater than 1000 km) of the model and Geosat have comparable amplitudes. The main differences between the model SSH and the Geosat ERM data occur over regions where seasonal steric variations are significant (from 20°N to 30°N). Wavenumber spectra over the Kuroshio Extension region reveal similar dynamics in both data sets. Much of the energy in wavenumber spectra appears as westward propagating SSH anomalies near the theoretical Rossby wave dispersion relations. As the Rossby wave dispersion relation changes with latitude (shifting to shorter wavelengths with higher latitudes), the peaks in the wavenumber decompositions follow. Thus the dynamics are generally consistent with quasi-geostrophic dynamics in both the model and altimeter data. Wavelengths of propagating SSH anomalies which have spectral peaks near the Rossby dispersion curve are longer in the Geosat and model than wavelengths indicated by theory. In the semiannual frequency below 35°N, westward propagation dominates over eastward propagation in both Geosat and the model. Most differences in the dynamics of the model and Geosat occur at shorter length and timescales, with Geosat showing higher amplitudes at the shorter scales than the model.				
14. SUBJECT TERMS  models, altimeter data			15. NUMBER OF PAGES 21	
			16. PRICE CODE	
17. SECURITY CLASSIFICATION OF REPORT Unclassified	18. SECURITY CLASSIFICATION OF THIS PAGE Unclassified	19. SECURITY CLASSIFICATION OF ABSTRACT Unclassified	20. LIMITATION OF ABSTRACT SAR	